

UNIVERSITY OF ZAGREB  
FACULTY OF MECHANICAL ENGINEERING AND NAVAL  
ARCHITECTURE

MASTER'S THESIS

Dajana Benković

ZAGREB, 2018

UNIVERSITY OF ZAGREB  
FACULTY OF MECHANICAL ENGINEERING AND NAVAL  
ARCHITECTURE

## MASTER'S THESIS

NUMERICAL MODELLING OF THE GASOLINE FUEL INJECTION  
PROCESS UNDER THE FLASH BOILING CONDITIONS

Mentor:

Asst. prof. dr. sc. Milan Vujanović

Student:

Dajana Benković

ZAGREB, 2018



SVEUČILIŠTE U ZAGREBU  
**FAKULTET STROJARSTVA I BRODOGRADNJE**  
Središnje povjerenstvo za završne i diplomske ispite  
Povjerenstvo za završne i diplomske ispite studija zrakoplovstva



Sveučilište u Zagrebu Fakultet strojarstva i brodogradnje	
Datum	Prilog
Klasa:	
Ur.broj:	

## DIPLOMSKI ZADATAK

Student: **Dajana Benković**

Mat. br.: 0035185910

Naslov rada na  
hrvatskom jeziku:

**Numeričko modeliranje procesa ubrizgavanja i isparavanja goriva u  
uvjetima povišene temperature goriva i niskog tlaka komore izgaranja**

Naslov rada na  
engleskom jeziku:

**Numerical Modelling of the Gasoline Fuel Injection Process Under the  
Flash Boiling Conditions**

Opis zadatka:

Korištenje računalne dinamike fluida (RDF) u kombinaciji s eksperimentalnim pristupom postao je uobičajen pristup u razvoju različitih inženjerskih sustava, kao što su motori s unutrašnjim izgaranjem. Moderni benzinski motori korišteni u zrakoplovima generalne avijacije koriste sustave ubrizgavanja goriva, što predstavlja područje prikladno za primjenu RDF-a. Poznato je da efikasnost motora s unutrašnjim izgaranjem ovisi o procesu ubrizgavanja. Razumijevanje i modeliranje fizikalnih fenomena koji se pojavljuju pri određenim radnim točkama motora omogućuje razvoj konstrukcije koja zadovoljava kriterije visoke iskoristivosti i pouzdanosti, posebno bitnih u zrakoplovnom inženjerstvu. Unutar ovog rada, potrebno je izračunati proces ubrizgavanja i isparavanja benzinskog goriva pri uvjetima povišene temperature goriva i niskog tlaka komore izgaranja. Potrebno je analizirati navedene procese koji nastaju unutar same sapnice. U okviru rada, kandidat mora napraviti sljedeće:

1. Opisati osnovne jednadžbe računalne dinamike fluida te opisati jednadžbe korištene za opisivanje procesa ubrizgavanja goriva;
2. Generirati pomičnu računalnu domenu brizgaljke;
3. Prikazati numeričke postavke koje će se koristiti za rješavanje problema;
4. Računalno modelirati proces ubrizgavanja i isparavanja goriva;
5. Obrazložiti izračunate rezultate.

Sva potrebna literatura, opis modela te ulazni i početni podaci za analizu slučaja bit će dostupni od strane mentora i neposrednog voditelja.

U radu je potrebno navesti korištenu literaturu i eventualno dobivenu pomoć.

Zadatak zadan:

Rok predaje rada:

Predviđeni datumi obrane:

27. rujna 2018.


29. studenoga 2018.

5., 6. i 7. prosinca 2018.

Zadatak zadao:

Predsjednik Povjerenstva:

  
Doc. dr. sc. Milan Vujanović

  
Prof. dr. sc. Ivica Smojver

*I would like to express my gratitude to Professor Milan Vujanović for giving me an opportunity to work in his team, and for being the thesis supervisor.*

*I am trully thankful to Dr. Zvonimir Petranović, for sharing his knowledge and gouiding me all the way through the thesis.*

*Also, I would like to thank the CFD development group from AVL-AST, Graz, Austria.*

*Special thanks to my friends and colleagues for making my student time worth remembering.*

*Last but not least, I would like to thank my greatest fans, my parents, for their understanding, patience and every form of support there is.*

## **Statement | Izjava**

I hereby declare that I have made this thesis independently using the knowledge acquired during my studies and the cited references.

Izjavljujem da sam ovaj rad radila samostalno koristeći znanja stečena tijekom studija i navedenu literaturu.

Zagreb, 2018

Dajana Benković

# Contents

List of Figures	III
List of Tables	V
List of Symbols	VI
Sažetak	X
Abstract	XI
Prošireni sažetak	XII
<b>1. Introduction</b>	<b>1</b>
1.1. Historical development of piston engines . . . . .	1
1.2. Aircraft fuel systems . . . . .	3
1.2.1. Fuel injection systems . . . . .	4
<b>2. Mathematical model</b>	<b>10</b>
2.1. Mass conservation law . . . . .	10
2.2. Momentum conservation law . . . . .	11
2.3. Energy conservation law . . . . .	11
2.4. Turbulence modelling . . . . .	12
2.4.1. $k - \zeta - f$ turbulence model . . . . .	12
2.5. Mass transfer modelling . . . . .	13
2.5.1. Non-Linear Cavitation Model . . . . .	13
2.5.2. Flash Boiling model . . . . .	15
2.6. Momentum transfer modelling . . . . .	16

2.6.1. Cavitation Drag Model . . . . .	16
2.6.2. Gas Liquid System 3 . . . . .	17
2.7. Enthalpy transfer modelling . . . . .	17
2.7.1. Ranz-Marshall 2 . . . . .	17
<b>3. Computational mesh and numerical setup</b>	<b>19</b>
3.1. Structured computational mesh . . . . .	19
3.2. Boundary and initial conditions . . . . .	22
3.3. <i>Nozzle file</i> configuration . . . . .	26
3.4. Numerical simulation setup . . . . .	28
<b>4. Results</b>	<b>31</b>
<b>5. Conclusion</b>	<b>47</b>
<b>Bibliography</b>	<b>49</b>
<b>A. Appendix</b>	<b>53</b>

# List of Figures

1.1	Flash boiling phases . . . . .	5
1.2	Bubble growth . . . . .	6
3.1	GDI injector surface . . . . .	19
3.2	GDI injector computational mesh . . . . .	20
3.3	Details of GDI injector computational mesh . . . . .	20
3.4	a) Selections for mesh movement, b) mesh refinement . . . . .	21
3.5	a) Needle lift curve, b) needle positions for $\Delta Y=0\mu\text{m}$ , $\Delta Y=25\mu\text{m}$ and $\Delta Y=54\mu\text{m}$ . . . . .	21
3.6	Selections for boundary conditions . . . . .	22
3.7	Selections for nitrogen initial conditions . . . . .	25
3.8	Initialization methodology . . . . .	26
3.9	Selections for <i>Nozzle file</i> generation . . . . .	28
4.1	Total mass flow rate of standard Spray G calculation compared with experimental results . . . . .	32
4.2	Mass flow rate of each nozzle for standard Spray G calculation . . . . .	32
4.3	Total mass flow rate of Spray G flash boiling calculation . . . . .	33
4.4	Mass flow rate of each nozzle for Spray G flash boiling calculation . . . . .	33
4.5	Injected mass: hole-to-hole variation . . . . .	34
4.6	Standard Spray G liquid phase volume fraction at the early stage of injection . . . . .	35
4.7	Spray G liquid phase penetration . . . . .	36
4.8	Standard Spray G operating condition: hole-to-hole variation taken for the liquid phase at $400\mu\text{s}$ after the start of the injection . . . . .	37
4.9	Standard Spray G vapour volume fraction at the early stage of injection . . . . .	37



4.10 Spray G liquid phase velocity field . . . . .	38
4.11 Spray G2 liquid phase volume fraction at early stage of injection . . . . .	39
4.12 Spray G2 liquid phase development . . . . .	39
4.13 Spray G2 liquid phase velocity field . . . . .	40
4.14 Spray G2 vapour volume fraction at the early stage of injection . . . . .	41
4.15 Development of a Spray G2 vapour phase volume fraction . . . . .	42
4.16 Spray G2 vapour phase velocity at the first half of injection process . . . .	43
4.17 a) Iso-surface of vapour volume fraction taken in the middle of simulation ( $t=400 \mu s$ ), b) experimental imaging . . . . .	43
4.18 Vapour generated at low lift conditions near the end of injection at 760 $\mu s$ in Spray G2 simulation performed in: a) FIRE AVL <sup>TM</sup> , b) OpenFOAM	44
4.19 String-cavitation appearance in the upper nozzle region . . . . .	45
4.20 Liquid volume fraction comparison of Spray G and Spray G2 simulations	45
4.21 Vapour volume fraction comparison of Spray G and Spray G2 simulations	46

# List of Tables

3.1	Fluid properties . . . . .	23
3.2	Boundary conditions . . . . .	24
3.3	Initial conditions . . . . .	26
3.4	<i>Nozzle file</i> structure . . . . .	27
3.5	Underrelaxation factors . . . . .	29
3.6	Convergence criteria . . . . .	30
4.1	Hole-to-hole variation in mass flow and according discharge coefficients .	34

# List of Symbols

## Greek Symbols

$\alpha$	-	Volume fraction
$\chi$	-	Underrelaxation factor
$\epsilon$	-	Void fraction
$\Gamma_{kl}$	kg/s	Source term due to interphase mass exchange
$\kappa_c$	W/(mK)	Conductivity
$\lambda_{ac}$	-	Accommodation coefficient
$\mu$	N/(m <sup>2</sup> s)	Molecular viscosity coefficient
$\mu_t$	N/(m <sup>2</sup> s)	Turbulent dynamic viscosity
$\nu$	m <sup>2</sup> /s	Kinematic viscosity
$\rho$	kg/m <sup>3</sup>	Density
$\tau_{ij}$	N/m <sup>2</sup>	Viscous stress tensor
$\varepsilon$	m <sup>2</sup> /s <sup>3</sup>	Turbulent kinetic energy dissipation rate
$\varphi$	variable	Generic scalar variable
$\zeta$	-	Velocity scale ratio

## Latin Symbols

$\mathbf{F}_L$	N	Lift force
----------------	---	------------

---

$\mathbf{F}_{WL}$	N	Wall lubrication force
$\mathbf{v}_r$	m/s	Relative velocity
$A'''$	m	Bubble surface area
$A_i'''$	-	Interfacial area density
$C_D$	-	Drag coefficient
$C_d$	-	Discharge coefficient
$C_E$	-	Egler coefficient
$C_e$	-	Cavitation enhancement factor
$C_H$	-	Shape deviation constant
$C_r$	-	Condensation reduction factor
$C_\mu$	-	Turbulence model constant
$C_{TD}$	-	Turbulent dispersion coefficient
$D_b$	m	Bubble diameter
$f$	m <sup>2</sup>	Element surface
$f_i$	N	Mass force
$h$	J/kg	Specific enthalpy
$H_{kl}$	(Jkg)/s	Source term due to exchange of energy
$k$	m <sup>2</sup> /s <sup>2</sup>	Turbulent kinetic energy
$L$	m	Length
$m_i$	kg/s	Mass flow of phase i
$M_{kli}$	(kgm)/s	Source term due to interfacial momentum exchange
$n$	-	Number of elements

---

---

$N'''$	-	Bubble number density
$N_0'''$	-	Initial bubble number density
$p$	Pa	Pressure
$p_{sat}$	Pa	Saturation pressure
$q$	W/m <sup>2</sup>	Heat flow
$R$	m	Bubble radius
$R_g$	J/(kgK)	Gas constant
$S_1, S_2$	variable	Flow attributes
$S_\varphi$	variable	Source term
$T$	$K$	Temperature
$t$	s	Time
$T_c$	°C	Superheated liquid temperature
$t_t$	s	Turbulent time
$T_{sat}$	°C	Saturate vapour temperature
$u, v, w$	m/s	Velocity components
$V_{bubble}$	m <sup>3</sup>	Vapour volume
$V_{liquid}$	m <sup>3</sup>	Liquid volume
$x_{cen}$	-	Element centre X coordinate
$x_{nor}$	-	Element vector normal X coordinate
$y_{cen}$	-	Element centre Y coordinate
$y_{nor}$	-	Element vector normal Y coordinate
$z_{cen}$	-	Element centre Z coordinate

---

$z_{nor}$  - Element vector normal Z coordinate

## Other Symbols

$\Delta p$  Pa Effective pressure difference

$\Delta T$  °C Degree of superheat

$\Delta Y$  m Needle lift

$Nu$  - Nusselt number

$Pr$  - Prandtl number

$Re_b$  - Local bubble Reynolds number

## Abbreviations

CDS Central Differencing Scheme

CFD Computational Fluid Dynamics

CFL Courant-Friedrichs-Lewy

ECN Engine Combustion Network

GDI Gasoline Direct Injection

RANS Reynolds Averaged Navier-Stokes

TDS Turbulent Dissipation Rate

TKE Turbulent Kinetic Energy

TLS Turbulent Length Scale

UDS Upwind Differencing Scheme

# Sažetak

Sigurnost i pouzdanost glavni su prioriteti u zrakoplovnoj industriji, zbog čega se teži ka usavršavanju svakog dijela te svakog procesa. Motori s unutarnjim sagorijevanjem ne predstavljaju iznimku: evolucija motora s unutarnjim sagorijevanjem za sobom povlači i razvoj te razumijevanje svakog segmenta procesa izgaranja motora. Sustav kojim se gorivo dovodi u komoru izgaranja predstavlja jedan od mnogih čimbenika koji izravno utječu na proces izgaranja. Nagli razvoj tehnologije ubrizgavanja goriva nudi mogućnost primjene brojnih prednosti takvog sustava dobave goriva. Iz tog razloga, korištenjem modernog inženjerskog alata u svrhu istraživanja raznovrsnih inženjerskih sustava - računalne dinamike fluida (RDF), ovaj rad obuhvaća numeričku analizu sustava direktnog ubrizgavanja goriva u *flash boiling* operativnim uvjetima motora. *Flash boiling* je pojava brzog smanjenja tlaka predgrijanje kapljevine na vrijednost tlaka manju od tlaka zasićenja kapljevine. Numerička analiza realne geometrije benzinske brizgaljke, provedena je unutar komercijalnog programskog paketa za računalnu dinamiku fluida AVL FIRE™. Kako bi se reproduciralo stvarno pomicanje dijelova brizgaljke tijekom procesa ubrizgavanja goriva, izrađena je pomična računalna domena. Definirane su numeričke postavke rješavača, uključujući i rubne te početne uvjete za oba promatrana slučaja: standardni te *flash boiling* slučaj. Nadalje, provedna je analiza dobivenih rezultata, nakog čega su dane usporedbe dvaju razmatranih režima procesa ubrizgavanja goriva. Rezultati *flash boiling* simulacije na kraju su uspoređeni s eksperimentalnim podacima te numeričkim rezultatima, utvrđenim iz proračuna provedenih u drugom računalnom kodu.

**Ključne riječi:** Flash Boiling, Spray G2, isparavanje goriva, direktno ubrizgavanje goriva, CFD

# Abstract

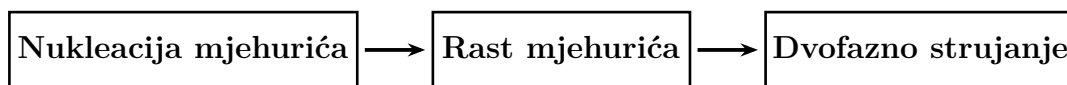
Safety and reliability are a priority in aerospace industry today and in the relentless pursuit for improvements every part and every process is scrutinized. Internal combustion engines are not an exception: evolution of the internal combustion engines includes understanding and development of every segment of the engine combustion process. The fuel delivery system represents one of the many factors which was found to have a direct impact on the combustion process. Due to the large-scale development of the fuel injection technology, many advantages of such fuel delivery system are recognized and applicable. For that reason, by using a modern engineering tool for investigation of various engineering systems—Computational Fluid Dynamics (CFD), a numerical analysis of the direct fuel injection system under the flash boiling operating conditions was performed in this thesis. Flash boiling is a phenomenon of preheated liquid depressurization to the value below the liquid saturation pressure. Numerical investigation of a gasoline injector was carried out in commercial computational fluid dynamics software AVL FIRE<sup>TM</sup>. In order to reproduce the actual movement of injector parts during the injection process, a moving computational domain was created. Numerical setup, that includes definitions of boundary and initial conditions, as well as the solver setup of both standard and flash boiling operating conditions, was presented. Postprocessing of obtained results was made afterwards, and the flash boiling case was compared with the standard one. Finally, the results of the flash boiling simulation were compared with the available experimental data and numerical results from the literature.

**Keywords:** Flash Boiling, Spray G2, fuel vaporization, direct fuel injection, CFD



# Prošireni sažetak

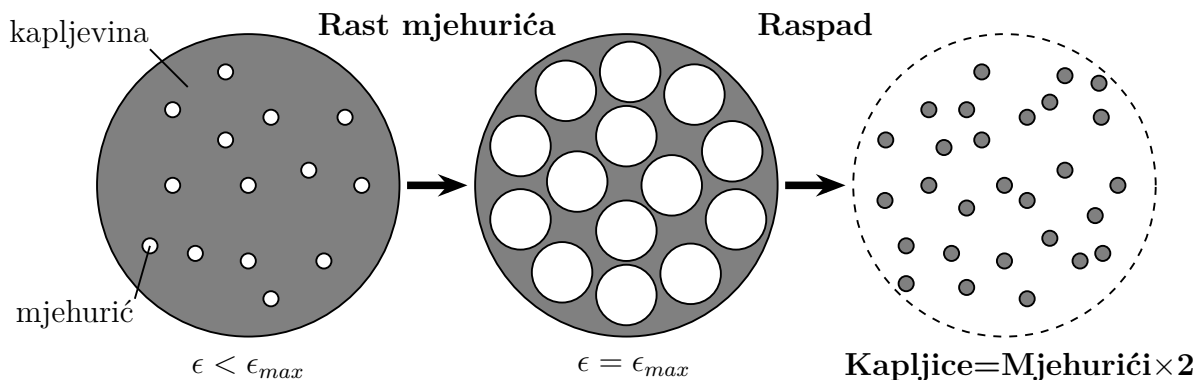
Upotrebom računalne dinamike fluida (RDF) provedena je analiza procesa izravnog ubrizgavanja benzinskog goriva. Ukoliko se predgrijana kapljevina ubrizgava u okolinu nižeg tlaka od tlaka zasićenja kapljevine, dolazi do stvaranja *flash boiling* uvjeta. U takvim uvjetima, sustav se nalazi u stanju termodinamičke neravnoteže. Ukoliko se tlak kapljevine spusti na vrijednost nižu od tlaka zasićenja iste, kapljevina se definira kao “pregrijana” te nastupa neposredno isparavanje. Proces je prikazan dijagramom na slici 0.1.



Slika 0.1: Faze *flash boiling* procesa [1]

Nakon što su stvorena područja nukleacije mjehurića, tlačne oscilacije kapljevine mogu uzrokovati njihov rast ili raspad. Rast mjehurića, prikazan slikom 0.2, prema [2] posjeduje navedene karakteristike:

- unutar mjehurića postoji jednolika raspodjela tlačnog i temperaturnog polja koje odgovara temperaturi goriva;
- mjehurići su sferičnog oblika;
- promjena kapljevite u parovitu fazu odvija se kontinuirano;
- prema Marangonijevoj konvenciji, frekvencija srastanja mjehurića tijekom njihovog rasta također raste.



Slika 0.2: Rast mjehurića [2]

Porast mjehurića unutar kapljica nije proizvoljan. Ograničen je znatnim brojem faktora kao što su promjer kapljice, površinska napetost, viskoznost kapljica, stopa rasta, itd. Sukladno tome, rast mjehurića opisan je udjelom pare  $\epsilon$  prema izrazu:

$$\epsilon = \frac{V_{bubble}}{V_{bubble} - V_{liquid}}, \quad (0.1)$$

gdje su  $V_{bubble}$  i  $V_{liquid}$  volumeni parovite i kapljevine faze. Razlika temperature goriva na izlazu iz brizgaljke te temperature zasićenja za tlak u komori izgaranja, predstavlja glavni parametar prema kojem se očituje pojava *flash boiling*-a. Ta temperaturna razlika označuje se s  $\Delta T_{sup}$  i naziva se stupanj pregrijavanja, a može se definirati i kao razlika između tlaka okoline i tlaka pare goriva [3]. Pokazano je da atomizacija mlaza nastupa ukoliko je stupanj pregrijavanja dovoljno velik da prouzroči *flash boiling*. Prema [3], *flash boiling* efekt uočen je u slučajevima kad je  $\Delta T_{sup} \geq 20^\circ$ .

## Matematički model

U računalnoj dinamici fluida, svaki problem svodi se na rješavanje zakona očuvanja proizvoljnog fizikalnog svojstva. Generalno, zakon očuvanja fizikalnog svojstva dan je jednačinom 0.1:

$$\frac{\partial (\rho \varphi)}{\partial t} + \frac{\partial}{\partial x_j} \left( \rho v_j \varphi - \Gamma \frac{\partial \varphi}{\partial x_j} \right) = S_\varphi, \quad (0.2)$$

gdje prvi član lijeve strane predstavlja brzinu promjene fizikalnog svojstva. Nadalje, članom u zagradi označene su konvekcija i difuzija, dok član na desnoj strani jednadžbe predstavlja izvorski član. Svi zakoni očuvanja korišteni unutar RDF-a predstavljaju specijalne slučajeve generalnog zakona očuvanja. Unutar ovog rada promatrano je višefazno strujanje fluida. Prisustvo različitih faza implicira da je za opis strujanja pored zakona očuvanja mase, količine gibanja i energije, potrebno zadovoljiti i jednadžbu kompatibilnosti koja govori da zbroj volumnih udjela svih faza unutar domene strujanja mora biti jednak jedan:

$$\sum_{k=1}^N \alpha_k = 1 \quad (0.3)$$

## Modeliranje turbulencije

Strujanje može biti laminarno, karakterizirano kao stabilno i uređeno, te turbulentno, kaotično strujanje. Turbulentno strujanje javlja se u prisustvu nestabilnosti i neuravnoteženosti strujanja. Strujanje u *flash boiling* uvjetima okarakterizirano je velikom neravnotežom tlaka i temperature, stoga je za potpuni matematički i numerički opis tog fenomena potrebno uzeti u obzir i modeliranje turbulencije. U tu svrhu korišteno je Reynoldsovo osrednjavanje Navier-Stokesovih jednadžbi. Specifično, korišten je  $k-\zeta-f$  model turbulencije. Taj model prigodan je za opisivanje procesa raspršivanja i vrtložnog strujanja, što je karakteristika motora s unutarnjim izgaranjem.

## Modeliranje prijenosa mase

U svrhu usporedbe, ispitano je isparavanje goriva u standardnim uvjetima te u *flash boiling* uvjetima. U slučaju standardnih uvjeta, izmjena mase između kontinuirane faze (kapljevine) te faze disperzije (pare) opisana je *Non-Linear Cavitation* modelom dok je za *flash boiling* uvjete korišten istoimeni model. Izmjena mase za standardni slučaj opisana je izrazom 0.4,

$$\Gamma_c = -\Gamma_d = \begin{cases} C_e \rho_d \left( 3\alpha_d^{2/3} (4\pi N''')^{1/3} \right) |\dot{R}| & \Delta p \geq 0 \\ -\frac{1}{C_r} \rho_d \left( 3\alpha_d \right)^{2/3} (4\pi N''')^{1/3} |\dot{R}| & \Delta p < 0 \end{cases} \quad (0.4)$$

u kojem empirijski koeficijenti  $C_e$  i  $C_r$  služe za regulaciju procesa isparavanja. U idealnom slučaju, njihove vrijednosti jednake su jedan.  $\alpha_d$  označuje volumni udio isparene faze, dok su s  $N'''$  i  $\dot{R}$  opisani gustoća mjehurića te vremenska derivacija njihovog radijusa [4]. U *flash boiling* modelu, međufazna razmjena mase opisana je izrazom 0.5, gdje  $\lambda_{ac}$  označuje faktor prilagodbe,  $A'''$  površinu mjehurića. S  $p_{sat}$  označen je tlak zasićenja kontinuirane faze.

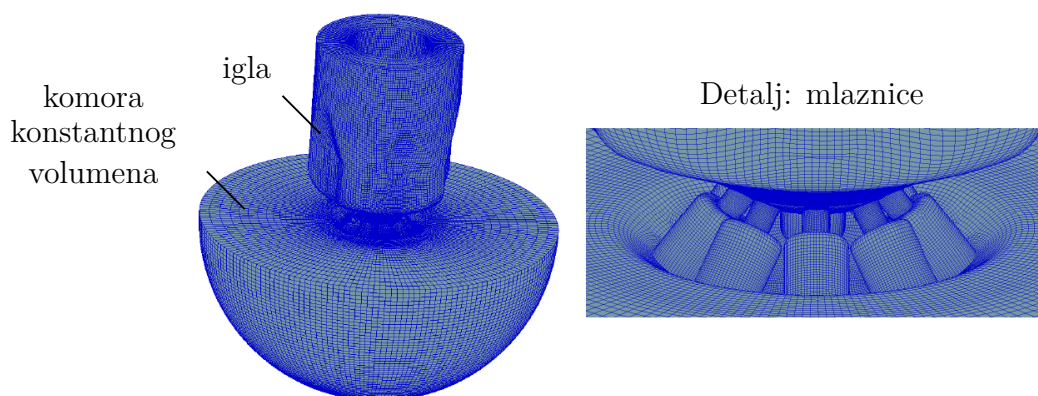
$$\Gamma_c = -\Gamma_d = \begin{cases} \lambda_{ac} C_e A''' |\dot{R}| & (p_{sat} - p) \geq 0 \\ -\frac{\lambda_{ac}}{C_r} A''' |\dot{R}| & (p_{sat} - p) < 0 \end{cases} \quad (0.5)$$

## Modeliranje prijenosa količine gibanja

Razmjena količine gibanja između kapljevite i parovite faze goriva opisana je *Cavitation Drag* modelom, dok je izmjena količine gibanja između dušika, prisutnog u komori izgaranja, te kapljevito goriva zadana modelom *Gas-Liquid 3* [4].

## Računalna domena i numeričke postavke

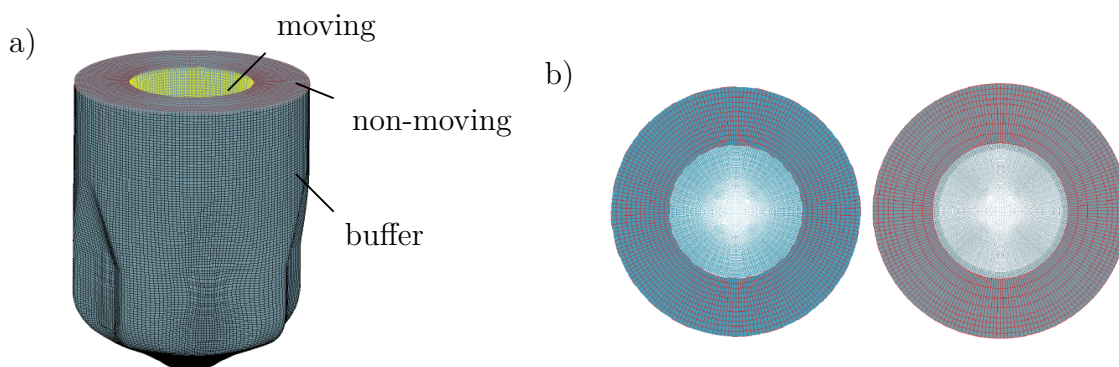
Računalna domena, prikazana slikom 0.3, izrađena je na temelju 3D modela izmjerene geometrije dostupne u [5]. Strukturirana mreža sastoji se od 1 233 920 kontrolnih volumena te se sastoji od tri dijela: igle i mlaznice brizgaljke te komore konstantnog volumena.



Slika 0.3: Strukturirana računalna domena brizgaljke

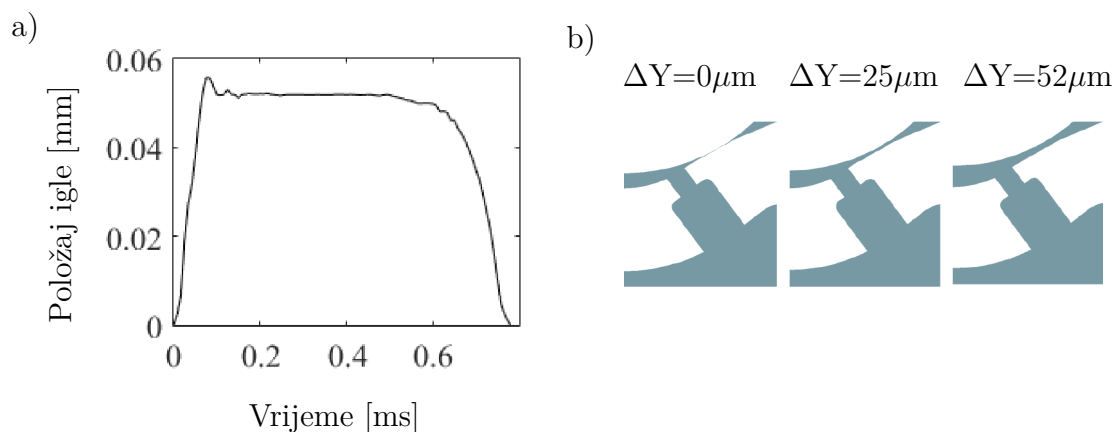
Prva računalna domena izrađena je kao nepomična, s iglom brizgaljke podignutom približno  $40\text{ }\mu\text{m}$  iznad sjedišta igle. U svrhu opisivanja stvarnog pomicanja dijelova brizgaljke tijekom procesa ubrizgavanja goriva (podizanje i spuštanje igle), igla brizgaljke u početnom trenutku mora biti spuštena do sjedišta. Iz tog razloga izrađene su selekcije na računalnoj domeni prikazane slikom 0.4 a). Tijelo brizgaljke izrađeno je u jednom dijelu, čiji poprečni presjek sadrži jednak broj raspodjela duž čitavog tijela brizgaljke. Takva geometrijska konfiguracija, uslijed spuštanja igle, dovela je do preklapanja kontrolnih volumena na najužem dijelu sjedišta ventila, te posljedično, do stvaranja negativnih volumena.

Problem je riješen prerađivanjem kritičnog dijela računalne domene, odnosno smanjenjem broja kontrolnih volumena duž poprečnog presjeka, kako je prikazano slikom 0.4 b).



Slika 0.4: a) Selekcije za izradu pomične računalne domene, b) prerađivanje računalne domene

Pomična računalna domena izrađena je pomoću “deformacijske formule” tako da je prvotno igla brizgaljke spuštena u zatvoreni položaj. Takva računalna domena je nadalje korištena kao početna te je pomicanje igle brizgaljke zadano prema eksperimentalno utvrđenoj krivulji [6]. Krivulja pomicanja igle, zajedno s prikazom različitih položaja iste, dana je slikom 0.5 a) i b).

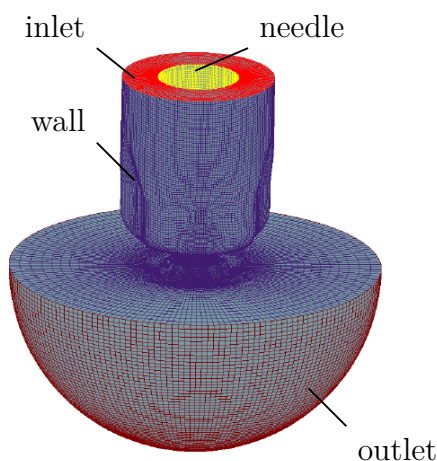


Slika 0.5: a) Krivulja pomicanja igle brizgaljke, b) Položaj igle brizgaljke za  $\Delta Y = 0 \mu\text{m}$ ,  $\Delta Y = 25 \mu\text{m}$  and  $\Delta Y = 54 \mu\text{m}$

## Rubni i početni uvjeti

Rubni i početni uvjeti zadani su na odgovarajućim površinskim selekcijama izrađenima na računalnoj domeni, slika 0.6. U svim simulacijama definirani su sljedeći rubni uvjeti:

- ulazna granica (definirana *inlet* selekcijom),
- izlazna granica (definirana *outlet* selekcijom),
- zid (definiran *wall* te *needle* selekcijom).



Slika 0.6: Selekcije za rubne uvjete

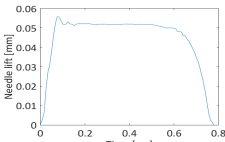
Strujanje unutar mlaznica modelirano je koristeći Eulerov višefazni model implementiran unutar programskog koda AVL FIRE<sup>TM</sup> koji omogućuje definiranje proizvoljnog broja promatranih faza. Svaka određena faza posjeduje jedinstveno rješenje brzine i turbulencije, dok je rješenje tlaka dijeljeno među fazama. Pošto se za svaku fazu rješava set diferencijalnih jednadžbi, rubni i početni uvjeti moraju se postaviti za sve definirane faze. Zadana svojstva fluida prikazana su u tablici 0.1.

Tablica 0.1: Svojstva fluida

<b>Faza 1: ISO-OCTANE</b>	
Koeficijent difuzije [-]	0.0257
Referentni tlak [Pa]	100 000
Referentna temperatura [K]	363
Turbulentni Schmidtov broj	0.9
<b>Faza 2: parovito gorivo</b>	
Gustoća [kg/m <sup>3</sup> ]	1.1
Dinamička viskoznost [Ns/m <sup>2</sup> ]	1.824e-5
<b>Faza 3: Dušik</b>	
Gustoća [kg/m <sup>3</sup> ]	3.5 (G) / 0.5 (G2)
Dinamička viskoznost [Ns/m <sup>2</sup> ]	1.824e-5

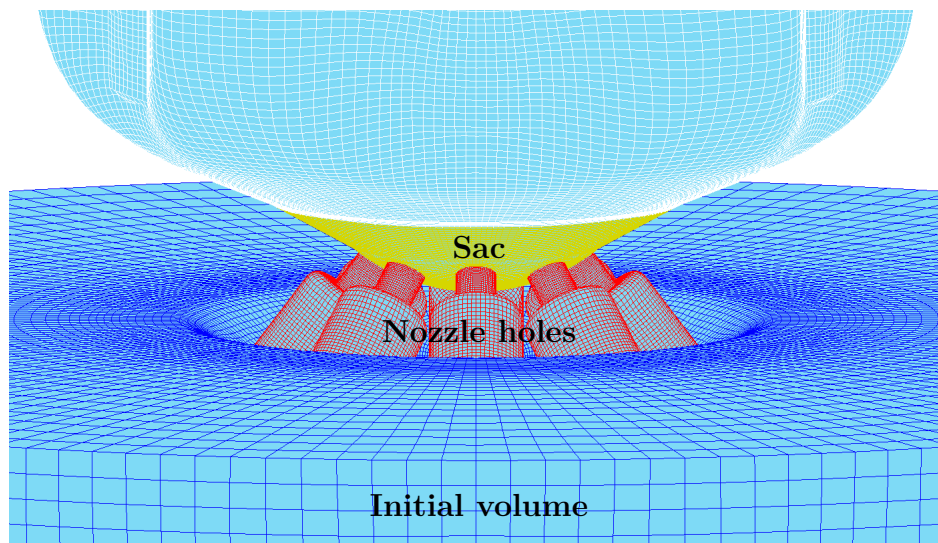
Numeričke postavke rubnih uvjeta definiranih za potrebe obaju simulacija prikazane su tablicom 0.2.

Tablica 0.2: Rubni uvjeti

	Faza 1	Faza 2	Faza 3
Inlet			
Tlak [bar]	200	-	-
Volumni udio [-]	0.999998	1e-6	1e-6
Temperatura [K]	363		
TKE [m <sup>2</sup> /s <sup>3</sup> ]	0.1		
TLS [m]	0.001		
Outlet			
Tlak [bar]	6 (G) / 0.5 (G2)	-	-
Volumni udio [-]	1e-6	1e-6	0.999998
Wall			
Termalno	Temperatura, 363 [K]		
Needle			
Termalno	Temperatura, 363 [K]		
Pomicanje	krivulja pomicanja igle 		

Početni uvjeti podijeljeni su na dva tipa: početne uvjete kapljevine te početne uvjete dušika. Početnim uvjetima kapljevine definira se stanje unutar čitave domene, dok je zadavanjem početnih uvjeta dušika određeno stanje plina okoline u određenom dijelu računalne domene. Kombinacijom početnih uvjeta moguće je postaviti položaj inicijalizacije određene faze. U ovom radu, korištenjem početnih uvjeta dušika varirana je inicijalizacija kapljevite faze. Kod provedenih simulacija, kapljevito gorivo inicijalizirano je do sjedišta ventila. Slikom 0.7 prikazane su selekcije kojima su pripisani početni uvjeti dušika. U tablici 0.3, dane su numeričke postavke početnih uvjeta korištenih u provedenim proračunima.





Slika 0.7: Selekcije za definiranje početnih uvjeta dušika

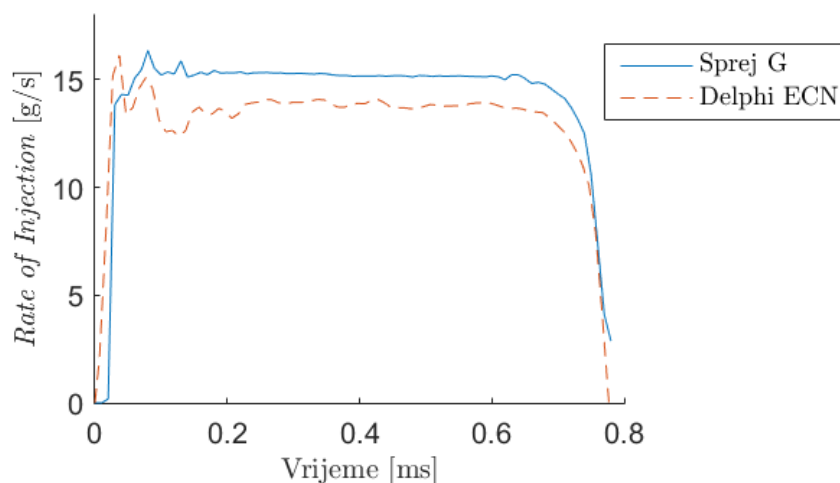
Tablica 0.3: Početni uvjeti

Početni uvjeti kapljevine			
	Faza 1	Faza 2	Faza 3
Tlak [bar]	200	-	-
Volumni udio [-]	0.999998	1e-6	1e-6
Temperatura [K]	363		
TKE [m <sup>2</sup> /s <sup>3</sup> ]	0.1		
TLS [m]	0.001		
Mod inicijalizacije	Uniforman		
Početni uvjeti dušika			
Tlak [bar]	6 (G) / 0.5 (G2)	-	-
Volumni udio [-]	1e-6	1e-6	0.999998
Temperatura [K]	573 (G) / 333 (G2)		
TKE [m <sup>2</sup> /s <sup>3</sup> ]	0.1		
TLS [m]	5e-5		
Mod inicijalizacije	Uniforman		

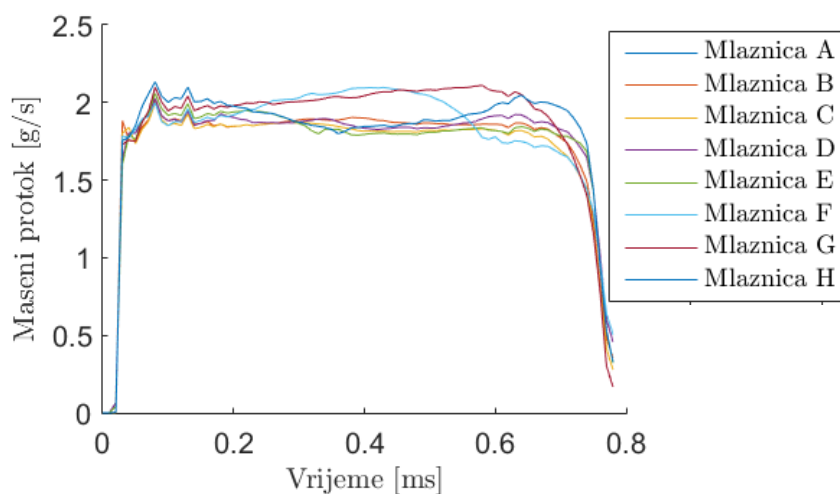
## Rezultati

Po završetku simulacija provedena je analiza rezultata procesa ubrizgavanja goriva u standardnim te *flash boiling* radnim uvjetima. Rezultati su prikazani u obliku dijagrama koji su dobiveni obradom podataka zapisanih po završetku simulacija u tzv. *Nozzle file*. *Nozzle file* je ASCII datoteka s \*.nzf ekstenzijom u koju se tijekom simulacije zapisuju podaci o promatranom strujanju, kao i podaci o računalnoj domeni. Prikazana je i usporedba 3D rezultata, obrađenih u programskom paketu AVL FIRE<sup>TM</sup>-u. Naposljetku, *flash boiling* slučaj uspoređen je s eksperimentom te proračunom provedenim u drugom računalnom kodu.

Krivulje prikazane dijagramima 0.8 i 0.9 predstavljaju maseni protok kapljevite faze tijekom čitavog procesa ubrizgavanja. Ukupan maseni protok standardnog slučaja uspoređen je s eksperimentom, slika 0.8, gdje je vidljivo da obje krivulje imaju jednak trend, kao i približno jednaku vršnu vrijednost. No numerički proces ubrizgavanja odvija se na nešto višim vrijednostima masenog protoka. Takvo ponašanje može se pripisati zanemarivanju poprečnih vibracija igle tijekom podizanja, pojednostavljenju geometrije te početnom položaju igle. Fluktuacije strujanja između pojedinih mlaznica vidljive su na dijagramu prikazanom na slici 0.9.

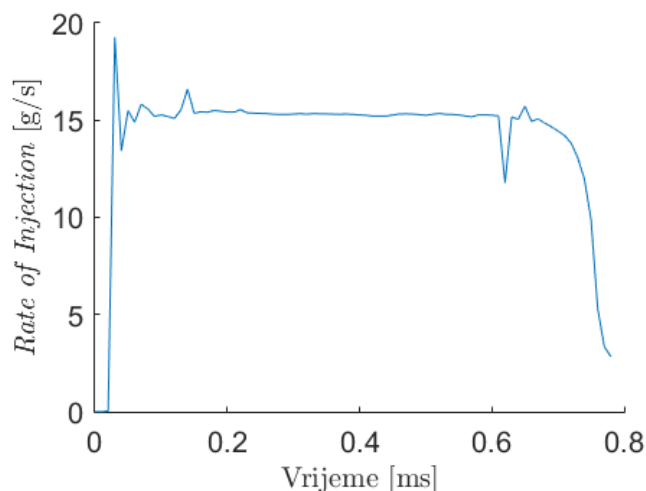


Slika 0.8: Ukupni maseni protok standardne Sprej G simulacije u usporedbi s eksperimentalnim rezultatima

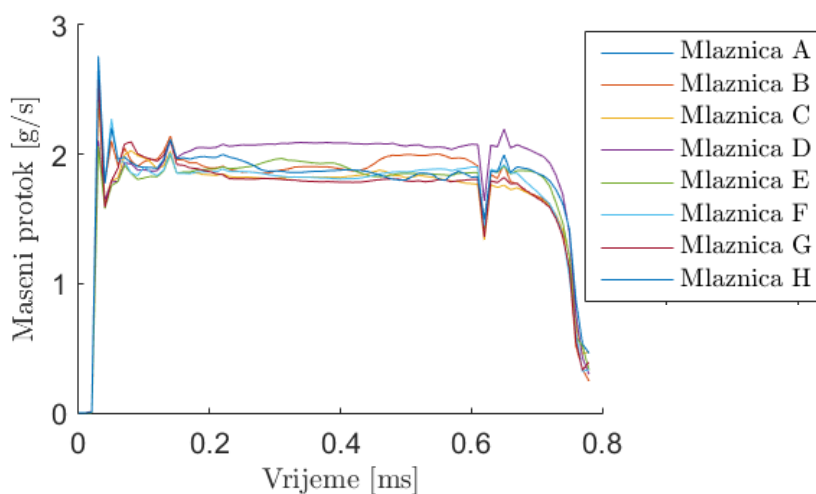
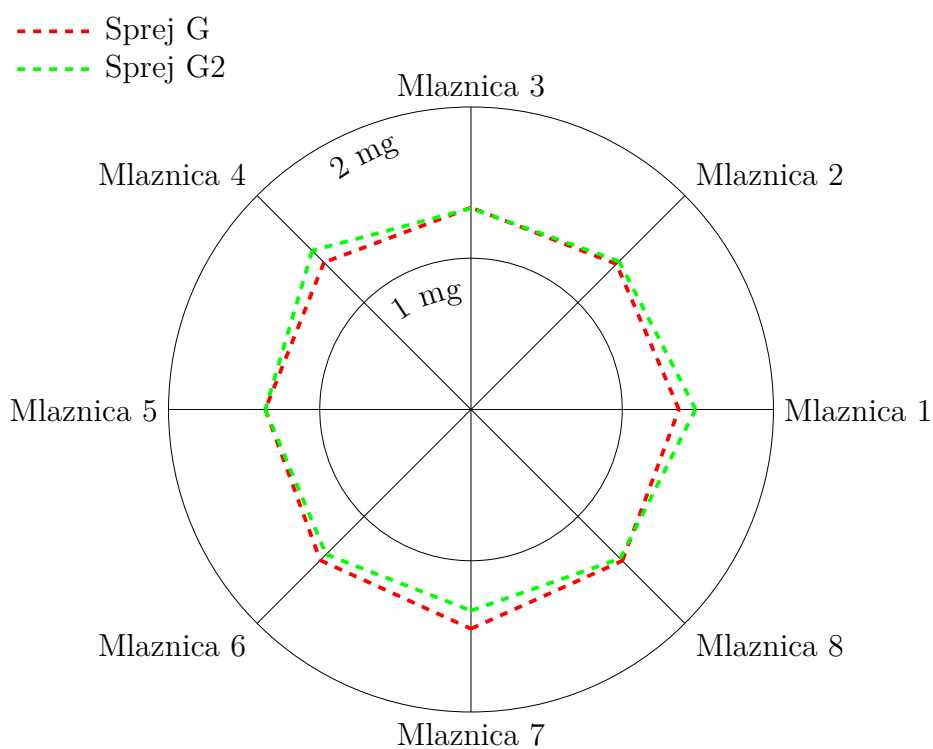


Slika 0.9: Maseni protok pojedine mlaznice za standardni Sprej G slučaj

Na jednak način, prikupljeni su te prikazani i rezultati procesa ubrizgavanja u *flash boiling* uvjetima, slike 0.10 i 0.11. U usporedbi sa standardnom simulacijom, početna vršna vrijednost masenog protoka nešto je viša, što je i očekivano s obzirom na veću razliku tlaka ubrizgavanja i tlaka komore. Približno  $600 \mu s$  nakon početka procesa ubrizgavanja primjećen je poremećaj kapljevite struje. Prethodno je utvrđeno da početak spuštanja igle uzrokuje narušavanje strujanja [7]. Maseni protok pojedinih mlaznica, slično kao i u standardnom slučaju, prati globalni trend uz prisutnost oscilacija.



Slika 0.10: Ukupni maseni protok za *flash boiling* slučaj

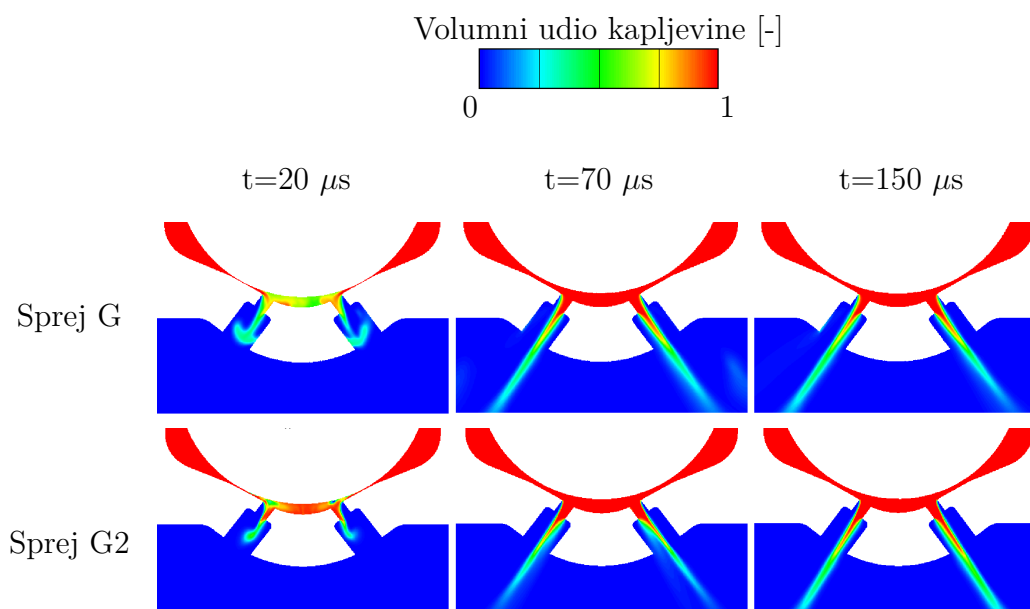
Slika 0.11: Maseni protok pojedine mlaznice za *flash boiling* slučaj

Slika 0.12: Ubrizgana masa: varijacija između mlaznica

Područje ispod prikazanih krivulja označava masu ubrizganog kapljevito goriva. Stoga je integriranjem individualnih te ukupnih krivulja ubrizgavanja izračunata ubrizgana masa goriva po mlaznici kao i ubrizgana masa goriva tijekom čitavog procesa. Za eksperimentalni slučaj, koji odgovara standardnom slučaju, ukupna masa ubrizganog goriva iznosi 10.16 mg.

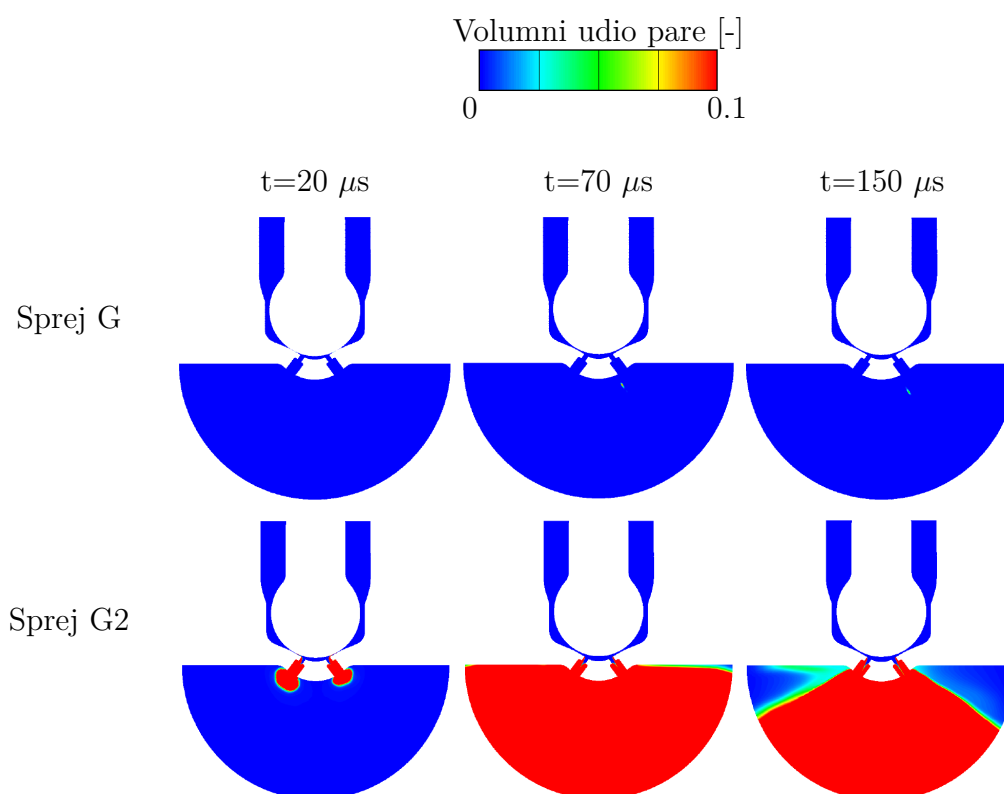
U numeričkom procesu ubrizgavanja, 11.08 mg kapljevito gorivo ubrizgano je u standardnim radnim uvjetima, dok ta masa u slučaju pojave *flash boiling*-a iznosi 11.12 mg. Dijagramom na slici 0.12, kvalitativno je prikazan utjecaj nesavršenosti geometrije na ubrizganu masu kapljevito goriva, ovisno o promatranoj mlaznici.

Usporedba standardnog i *flash boiling* slučaja prikazana je na slikama 0.13 i 0.14. Tako je na slici 0.13 prikazan razvoj kapljevine za oba slučaja gdje je vidljivo da prije nego što se strujanje stabilizira, u početku procesa ubrizgavanja, strujanje oscilira. U kasnijim stadijima procesa, raspodjela volumnog udjela kapljevine ujednačena je u oba slučaja.



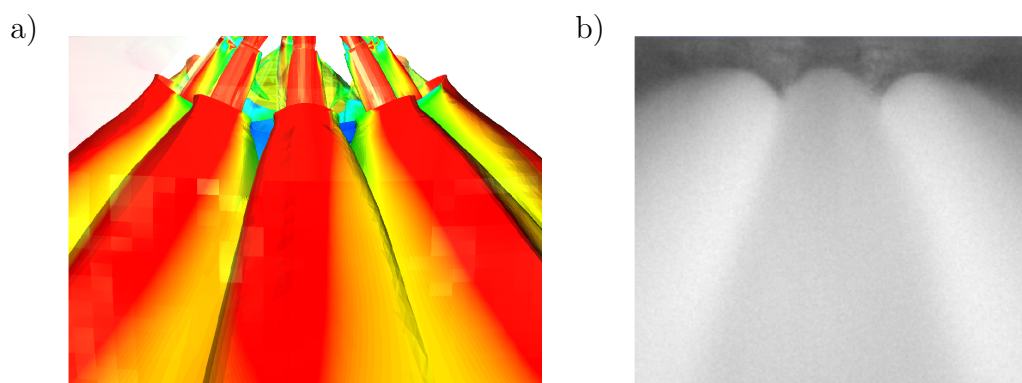
Slika 0.13: Usporedba volumnog udjela kapljevine za slučajeve Sprej G i Sprej G2

Za iste vremenske periode procesa ubrizgavanja prikazana je i parovita faza goriva, slika 0.14. U standardnom slučaju, para se pojavljuje periodično s vrlo malom vrijednošću volumnog udjela. U usporedbi s količinom pare koja se pojavljuje unutar *flash boiling* procesa, količina isparenog goriva u standardnom slučaju je zanemariva. S druge strane, proces isparavanja goriva u *flash boiling* slučaju odvija se gotovo trenutno. Čim para napusti mlaznice, dolazi do brze ekspanzije te se parovito gorivo nastavlja širiti po cijeloj domeni.



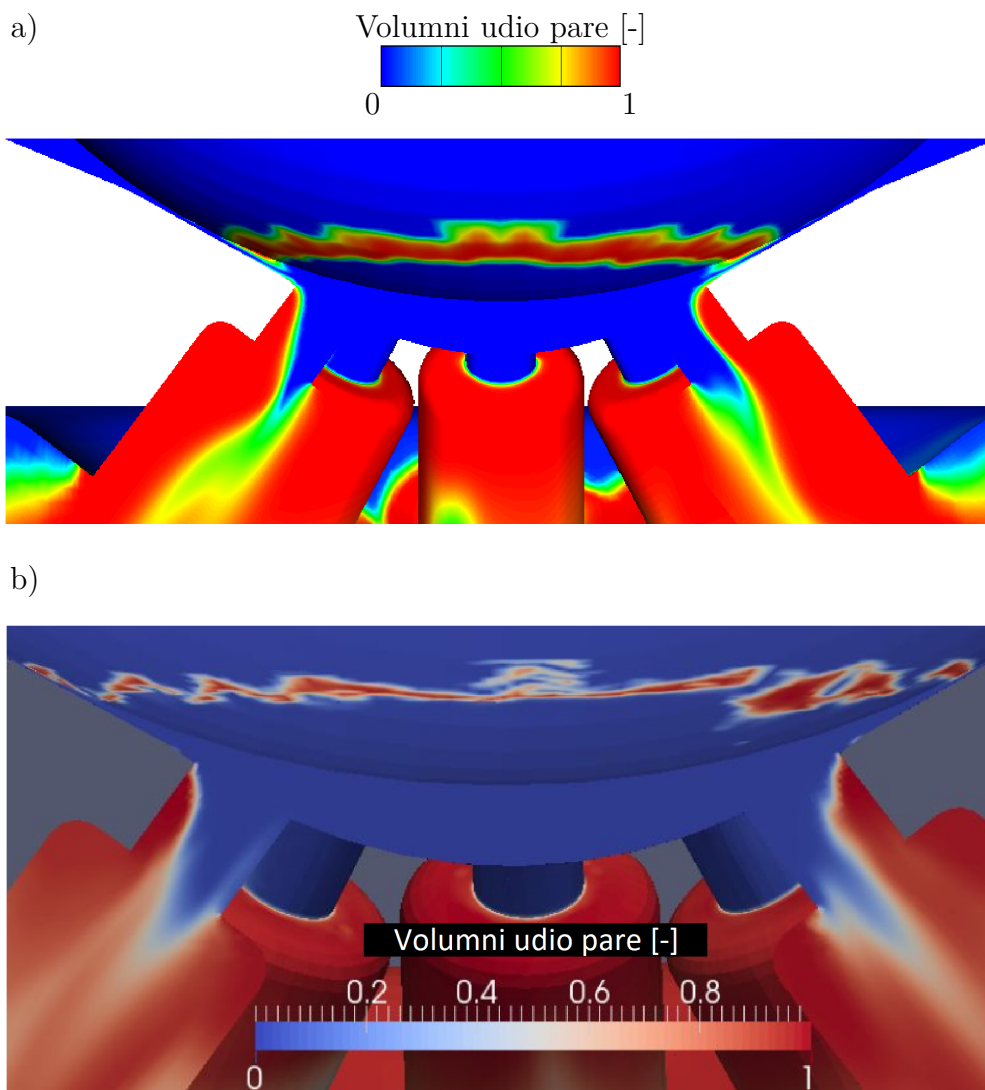
Slika 0.14: Usporedba volumnog udjela pare za slučajeve Sprej G i Sprej G2

*Flash boiling* simulacija uspoređena je s penetracijom spreja ECN GDI brizgaljke utvrđene eksperimentalnim snimanjem [7], što je prikazano na slici 0.15. Numerički rezultati dobro se poklapaju s eksperimentom u pogledu velikog kuta spreja koji rezultira međudjelovanjem između susjednih oblaka pare.



Slika 0.15: a) Izo-površina volumnog udjela parovite faze usred procesa ubrizgavanja ( $t=400 \mu s$ ), b) eksperimentalna snimka spreja [7]

Napravljena je i usporedba isparenog goriva u *flash boiling* radnim uvjetima, simuliranih u AVL FIRE™ te rezultata utvrđenih u OpenFOAM-u, [8]. Blizu završetka ubrizgavanja goriva (oko 760  $\mu$ s nakon početka procesa ubrizgavanja), raspodjela parovite faze na području sjedišta igle upućuje na pojavu tzv. *string* kavitacije, odnosno izduljenog kavitacijskog mjehura koji se proteže kroz sjedište igle te spaja mlaznice.



Slika 0.16: Ispareno gorivo prikazano za niski položaj igle brizgaljke, snimljeno 760  $\mu$ s nakon početka ubrizgavanja goriva u *flash boiling* radnim uvjetima, simulirano u: a) AVL FIRE™, b) OpenFOAM [7]

# 1 | Introduction

The history of aviation starts in 1903 with the Wright brothers and their first controlled, sustained flight of a powered heavier-than-air aircraft *Flyer I*. In the time that followed, development of civil, and especially military aviation reached an unexpected proportion: within the next hundred years, aircraft were enabled to uphold large-scale transport of passengers and cargo to long distance destinations. Aircraft have thus become an integral part of everyday life and a subject of continuous research and development.

In the days of early aviation, aircraft were powered by adapted automotive engines. Although this practice has become obsolete, the technology transfer of the aviation beginnings still offers some attractive prospects. Technology featured in direct-fuel injection engines is tested and validated. Safety and reliability, which are number one concerns in aviation today, could greatly benefit from the tried and true technology of yesterday. With the growth of the industry, a deeper understanding of direct injection systems and processes is offered, so the advantages of such technology are ready to found its purpose within the aircraft.

Computational fluid dynamics (CFD) is a modern engineering tool which accelerates the development of various engineering systems. Its prominent advantages over experiments include lower costs and possibility to investigate a large number of design solutions in a relatively short time. In this study the CFD tool AVL FIRE<sup>TM</sup> was employed to analyse the behaviour of the gasoline injector.

## 1.1. Historical development of piston engines

The first internal combustion piston engines were developed from steam engines. Automotive and aviation industry waited for the appearance of Daimler's motorcycle engine



and Benz's and Maybach's automotive engine in 1885, to meet the necessary conditions for their development. At the beginning of the 20th century, the aircraft engines were simple machines of low power and were constructed *ad hoc*, for a particular aircraft. With aviation development, the number of manufacturers, and consequently the number of manufactured engines started to grow.

Before their first controlled flight, the Wright brothers carried out experiments with gliders. Since there was no manufacturer who would construct an engine according to their requirements, they have build their own engine based on an automotive engine. That exact engine, weighing 82 kg and developing the output power of 12 HP, enabled the first successful powered heavier-than-air flight. The *Flyer I* engine had aluminium housing and had no carburettor, i.e. the fuel was continuously poured into the cylinders. Additionally, the engine was air-cooled, and the engine rotating speed was controlled by sliding the pre-burn point [9].

Further development of the aeronautical piston engines was marked by the usage of new materials, especially aluminium alloys. One of the first, and often used aircraft engines until 1910 was Antoinette, engine constructed by Levavasseur [9]. It was water cooled, eight-cylinder V engine, that generated the power of 50 HP and weighed 50 kg. That power-to-weight ratio was not exceeded for the next 25 years.

With its mass of 75 kg and output power of 50 HP, rotary engine Gnome Omega had an excellent power-to-weight ratio (mass of rotary engines was  $\frac{2}{3}$  mass of usual engines). One of the main advantages of rotary engines was a successful cooling solution. However, the engine had multiple disadvantages: great rotating mass due to the gyroscopic effect created problems during aircraft manoeuvres, as well as large ventilation losses. In addition, the engine had a large fuel and oil consumption and relatively short time between the overhaul. Despite those disadvantages, Gnome Omega was the first engine widely used in aircraft during the first years of the WWI [9]. Further development led to the row engine Liberty, engine constructed with the aim of mass production which soon began to dominate the market. Among the plenty of aircraft engines, Hispano-Suiza 8BE was considered to be the best. The 8BE was compact eight-cylinder, water cooled engine with great output power.

After the WWI, the surplus of war aircraft engines found their purpose in civil aviation, as well as in other branches of industry. Technology slowly continued to develop

and grow, until the beginning of the WWII which instantiated another surge: in a short period, a variety of new concepts and more powerful and durable aircraft engines was made. For instance, Supermarine Spitfire and Messerschmitt Bf 109 resulted from the technology contest, two very well known aircraft that played a big role and that were great opponents. Innovations such as elliptic wing at Spitfire, and automatic slats at Messerschmitt, have been introduced [10].

Along with the great novelties considering aircraft structure and production, engines that power these aeroplanes were considered to be the best engines of the time. British Rolls-Royce-Merlin was Spitfire's engine and is considered the best engine of WWII [10]. It had a small working volume, large output power, and in order to compensate the lower density air it was equipped with a supercharger. On the other side, there was German Daimler-Benz DB601, engine of Messerschmitt, which implemented the direct fuel injection. Thus, problems with the carburettors at high altitudes and during the aircraft manoeuvring were solved. However, both Merlin and Daimler-Benz had no competitors at the time [9].

Considering the subject of this work, the historical overview stops with the cessation of the fuel injection systems usage. The reason lies in the complexity of such technology and poor understanding of problematics of direct injection technology, back at the time. However, the direct fuel injection systems represent the state-of-the-art technology. Due to the small-scale geometry and its performance under a wide range of operating conditions, they pose an attractive possible solution.

## 1.2. Aircraft fuel systems

An important aspect of aircraft engines is the fuel delivery system that was evolving alongside the engine development. According to [11], systems ensuring the fuel supply in Otto aircraft engines can be roughly divided into:

- carburettors (Float-type, and Pressure-type), and
- fuel injection systems (Plunger-type, Continuous fuel, and Electronically controlled injection).

In carburettors, the fuel mixture is prepared before entering the cylinder. Float-type and pressure-type carburettors are the most common in aviation. The float-type carburettor consists of six subsystems that control the discharge fuel quantity depending on air flow that enters the cylinder. Pressure-type carburettors constitute a closed pressure system that delivers fuel, from the engine pump up to the exhaust nozzle. A large problem with carburettors is the difficulty of fuel delivery when the aircraft is manoeuvring. Also, the tendency of ice formation represents a major issue. Another disadvantage is overheating of particular cylinders due to uneven fuel mixture distribution [12].

On the other hand, direct fuel injection systems significantly reduce the chances of ice formation, since the temperature drop happens inside or near the cylinder. Fuel injection improves fuel distribution resulting in a better fuel efficiency. When the carburettors are used, due to poor control over the mixture, variations in fuel distribution between the cylinders are present. For that reason, carburettors usually need the richer mixture, so the cylinders working in the leanest regime could work normally [11].

### **1.2.1. Fuel injection systems**

Direct injection fuel systems are used in a great number of piston engines with the main goal of improving the flammable mixture quality. In this kind of systems, the air is delivered through the intake manifold while the fuel is dispersed in the combustion chamber [11]. Variations in the mixture homogeneity due to intake manifold length, another disadvantage of carburettors, is therefore eliminated.

Two main types of injection systems are known in the aviation: continuous and direct injection. In the continuous injection systems used today, fuel is delivered to each nozzle where it mixes with air. While the engine is powered off, the fuel passage way towards the nozzles is closed, and the fuel lines stay filled with fuel [13]. After the WWII, development of direct fuel injection technology was abandoned because of its complexity and technological difficulties and it is the main reason that this technology is not used today [10].

However, the fuel injection technology is experiencing large-scale development today and there are many new advantages offered by that fuel delivery system. Within this work the Delphi solenoid injector used by the Engine Combustion Network (ECN) community, a group for international collaboration among experimental and computational

researchers in engine combustion, was utilized as a subject of interest. A fuel injector, called “Spray G”, is a stepped hole valve covered orifice (SVCO) 8-hole type injector with an outer cone angle of  $80^\circ$  [5]. The main subject of this thesis is investigation of fuel injection of that particular injector operating under the flash boiling (G2) conditions.

### Flash boiling (Spray G2) condition

Phenomenon when the preheated liquid is depressurized to the value below the liquid saturation pressure is known as flash boiling. A system in that kind of state is in a thermodynamic imbalance. In other words, the system is unstable. Therefore, if the liquid pressure decreases below its saturation pressure, a rapid liquid vaporization occurs. In a condition like that, fuel is defined as “superheated”. According to [1], three phases of flash boiling are known, as shown in Figure 1.1.

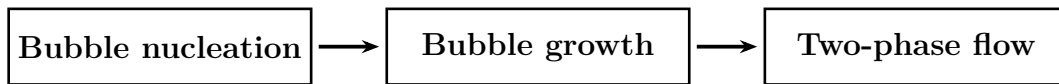


Figure 1.1: Flash boiling phases [1]

First phase, the bubble nucleation classifies into two groups:

- homogeneous - nucleation areas are formed inside the liquid, in the absence of bubble nuclei, with the homogeneous distribution. The homogeneous process becomes dominant when the liquid pressure is significantly reduced.
- heterogeneous - nucleation areas are formed when the gaseous and solid phases occur at the interface or, in a boundary layer instead of in a liquid. Nuclei can appear due to the surface irregularity (interior injector wall), fine dust or solid particles, as well as the dissolved gases in the liquid.

Once the nucleation areas are developed, pressure fluctuations of the fluid can cause their growth or collapse. According to [2], bubble growth, depicted in Figure 1.2 is described with the following:

- inside the bubble, there is a uniform distribution of the pressure and temperature which corresponds to the fuel temperature,
- the bubbles are growing spherically,

- change from the liquid to the gaseous phase occurs continuously as the bubbles are growing due to the cavity in the nozzle hole,
- according to the Marangoni convection, an increase in a coalescence frequency of a growing bubbles is present.

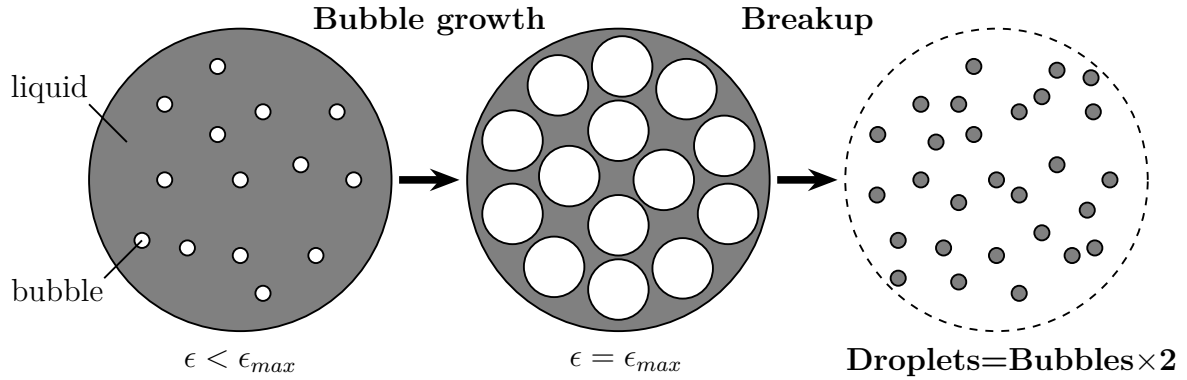


Figure 1.2: Bubble growth [2]

The bubble growth inside the droplets is not a random process. It is governed by a variety of factors, such as droplet diameter, surface tension, droplet viscosity, density number of bubble nuclei, growth rate, etc. The bubble growth is described with a void fraction  $\epsilon$ , given with the following expression:

$$\epsilon = \frac{V_{bubble}}{V_{bubble} - V_{liquid}}, \quad (1.1)$$

where  $V_{bubble}$  and  $V_{liquid}$  are representing the volumes of bubbles (gaseous phase) and liquid. Authors in [14] determined that the fuel jet decomposition happens for void fraction in a range from 0.51 - 0.53. Hence, the fuel “parent” droplets break into “children” droplets, half in size when compared to the parent droplets. After the decomposition, it is possible to calculate the number and diameter of newly created droplets. Additionally, the momentum is evenly distributed between the child droplets. Once the flash boiling process finishes, flow balance between the liquid and vapour is established.

In the direct injection engines, flash boiling can occur as a consequence of an overloading of particular parts [15], for example in following events:

- the fuel temperature is high ( $> 100^\circ\text{C}$ ) due to the heat conduction from the piston head,

- in the period of closed valves when the piston is moving downwards and the partial vacuum is created (up to the 0.1 bar),
- the fuel vaporization temperature at cylinder pressure is below the fuel temperature within the injector,
- preheated fuel is injected into the cylinder, and
- rapid and explosive bubble growth appears inside of the droplet and vaporizes the fuel.

By investigating the flash boiling process, Van der Wege [16] established 2 regimes of flash boiling: internal and external. Internal vaporization occurs when the bubbles are formed inside the injector hole, after which the emergence of a two-phase flow (liquid + vapour) follows. As it exits the injector, spray expands very quickly. In contrast, external vaporization happens in cases when the liquid jet, leaving the injector, stays intact. However, it breaks as the bubbles are growing while moving down the nozzle.

The main parameter for flash boiling appearance is the temperature difference of fuel exiting the injector and the fuel vaporization temperature for the chamber pressure condition in which fuel expands. That temperature difference is given by the term  $\Delta T_{sup}$ , and is called the degree of superheat. It is shown that the jet atomization acts when the degree of superheat is great enough to cause the flash boiling effect [17]. With further investigation of the degree of superheat, carried out in [3], it is determined that flash boiling occurs if  $\Delta T_{sup} \geq 20^\circ$ . However, the real value of  $\Delta T_{sup}$  depends on surface finish of the nozzle and Weber number. Degree of superheat can also be defined as the difference of the ambient pressure and fluid vapour pressure. By investigating the influence of nozzle geometry, authors in [18] and [19] introduced a length-to-diameter ( $L/D$ ) ratio as a factor that leads to fuel flashing. Also, by merging certain fuel properties, low-boiling and high-boiling fuel components [20], the evaporation tendency increases. Thus, the multicomponent fuels, such as gasoline, are more prone to flash boiling than the single-component fuels.

Apart from the causes of a flash boiling process, many researchers analysed such condition inside the cylinder to examine the effects of flash boiling on the injection process, and many conclusions were derived. For instance, in [21] and [22], authors

analysed the flash boiling operating condition under the transient needle motion and under three fixed needle lift positions. CONVERGE CFD package was used for the numerical simulation and the results were compared to the experimental data. Numerical results showed good agreement with the experimental imaging in terms of fuel mass fraction distribution inside the combustion chamber. Thus, the results of flash boiling calculations resolved the existence of uniform contact of fuel with the counter bores. Also, the hole-to-hole variations were examined and as a result, a small deviation of 2-3% in the injected fuel, between the simulation and experiment was obtained. It was determined that low needle lift, at the beginning and the end of a process, significantly affects the flow patterns in terms of local vapour distributions.

Baldwin [7] determined that at the low needle lift, an appearance of vapour occurs at the narrowest passage (needle seat position) of the computational domain. Injector sac filled with the fuel was analysed as well, and transient interacting vortices were found. Flow behaviour like that results in a string flash boiling appearance, perturbations in spray angle and directions, together with the oscillations in mass flow rate. Oscillations in the mass flow rate were attributed to the presence of vapour inside the nozzle holes which was also confirmed in [23]. Analysing the flash boiling operating conditions in OpenFOAM [24], it was shown that the injector geometry impacts the vapour formation at the nozzle inlet. Therefore, the increase of inlet radii decreases the cavitation formation at the nozzle entrance. In other words, a sharper inlet edge (smaller inlet radii) means a larger fluid turning angle as it enters the nozzle, hence creating a cavitation region.

Authors in [25] performed an experimental investigation of a five-hole gasoline direct injector spray collapse under flash boiling conditions. Spray morphology and droplet dynamics were examined by using the high-speed imaging and phase Doppler measurement technique. It was determined that spray collapse happens in the far field, which is attributed to the formation of a low-pressure zone due to the temperature decrease and the resulting condensation. Furthermore, at the inner side of a target jet, i.e. closer to the injector axis, a slight increase in the droplet size was noticed. Another experimental research of a direct fuel injection was carried out in [26] and [8], where the spray behaviour was captured by optical imaging. It was found that in order to reach the chamber pressure, fuel flow inside of the nozzle has to expand rapidly, consequently

vaporizing inside the counterbores. Further expansion of vaporized fuel prevents the downstream gas from entering the counterbores, and as a consequence, spreading of plume angle occurs. In case when the fuel expansion is significant, neighbouring spray plumes are able to interfere: plume-to-plume interaction in most cases leads to the spray collapse.

Effects of a flash boiling condition on a spray breakup were investigated in [27],[28]. It was established that the level of superheat is the main factor which determines the efficiency of spray atomization. Other fluid properties, such as viscosity and surface tension, were proved to enhance the effect of spray formation and break-up.

In this thesis, numerical analyses of a direct fuel injection system are carried out. Using previously described fuel injector geometry, flash boiling operating conditions were examined and compared with the standard operating conditions of a Spray G injector. This work is structured as follows. First in Chapter 2., the mathematical model used for performing a numerical investigation of direct fuel injection system, implemented within the commercial AVL FIRE<sup>TM</sup> CFD software, is described. Secondly, numerical simulation setup, regarding the meshing process and solver settings, is presented in Chapter 3.. The results are presented and discussed in Chapter 4.. In Chapter 5., the conclusions are derived.



## 2 Mathematical model

In order to perform numerical simulations, a great number of equations need to be solved. In Computer Fluid Dynamics (CFD) every problem comes down to solving the conservation laws of various physical properties. In general, conservation law of physical property is given with Equation 2.1, and it states: Rate of change of physical property in control volume equals to source or sink of physical property and the property flux balance through the volume boundaries.

$$\frac{\partial (\rho\varphi)}{\partial t} + \frac{\partial}{\partial x_j} \left( \rho v_j \varphi - \Gamma \frac{\partial \varphi}{\partial x_j} \right) = S_\varphi \quad (2.1)$$

The first term on the left-hand side describes the rate of change of physical property. The second term marks the convection and diffusion, while the right-hand side contains the source or sink terms. All other conservation laws used in the computational fluid dynamics are derivatives from the general conservation law. In other words, all conservation equations are special cases of general conservation equation. In continuation, fundamental conservation laws are given: continuity equation, momentum equation and energy equation. Additionally, the turbulence model is described, and models for definition of mass, momentum and enthalpy interfacial exchange are presented.

### 2.1. Mass conservation law

Within the multiphase model, conservation of mass or continuity equation states:

$$\frac{\partial (\rho_k \alpha_k)}{\partial t} + \frac{\partial (\rho_k \alpha_k v_{kj})}{\partial x_j} = \sum_{l=1, l \neq k}^N \Gamma_{kl}, \quad k = 1, \dots, N. \quad (2.2)$$

In Equation 2.2,  $\alpha_k$  is the volume fraction of the observed phase, while  $v_j$  describes velocity.  $\Gamma_{kl}$  represents the mass exchange between particular phases. With the continuity equation, given with the expression 2.3, the compatibility condition needs to be satisfied as well.

$$\sum_{k=1}^N \alpha_k = 1 \quad (2.3)$$

## 2.2. Momentum conservation law

Differential form of the momentum conservation law is given with the Equation 2.4, and states: the rate of change of momentum within the control volume equals to the sum of the external mass forces and surface forces acting upon the control volume.

$$\begin{aligned} \frac{\partial (\rho_k \alpha_k v_{ki})}{\partial t} + \frac{\partial (\rho_k \alpha_k v_{kj} v_{ki})}{\partial x_j} = & \alpha_k \frac{\partial}{\partial x_j} (-p \delta_{ji} + \Sigma_{ji}) + \alpha_k \rho_k f_i \\ & + \sum_{l=1, l \neq k}^N M_{kli} + \sum_{l=1, l \neq k}^N v_{ki} \Gamma_{kl} \end{aligned} \quad (2.4)$$

The left-hand side of the equation describes temporal and spatial change of the momentum. With the first term on the right side, the surface forces due to pressure and the fluid viscosity are given. The viscous stress tensor for the Newtonian fluid is described with expression:

$$\tau_{ji} = \mu \left( \frac{\partial v_j}{\partial x_i} + \frac{\partial v_i}{\partial x_j} \right) - \frac{2}{3} \mu \frac{\partial v_k}{\partial x_k} \delta_{ij}. \quad (2.5)$$

Kronecker delta,  $\delta_{ij}$  is mathematical operator that equals to 1 in case of  $i = j$ , while for  $i \neq j$  equals zero. Second term on the right-hand side of the Equation 2.4 contains mass forces, and with the third and fourth term, the momentum exchange between the phases is given.

## 2.3. Energy conservation law

With Equation 2.6, the energy conservation law is given, stating that the rate of change of kinetic and internal energy within the control volume equals to sum of power and the rate of change of the external and surface forces acting on that control volume, and the

rate of change of the heat between the control volume and environment.

$$\begin{aligned}
\frac{\partial (\alpha_k \rho_k h_k)}{\partial t} + \frac{\partial (\alpha_k \rho_k v_j h)}{\partial x_j} = & \frac{\partial}{\partial x_j} \left( \alpha_k (q_{kl} + q_{kj}^T) \right) + \alpha_k \rho_k \Theta_k + \alpha_k \delta_k f_j \cdot v_{ki} \\
& + \frac{\partial}{\partial x_j} \left( \alpha_k v_{ki} (\tau_{kij} + \tau_{kij}^T) \right) + \alpha_k \frac{\partial p}{\partial t} \\
& + \sum_{l=1, l \neq k}^N H_{kl} + \sum_{l=1, l \neq k}^N h_{kl} \Gamma_{kl}
\end{aligned} \tag{2.6}$$

The left-hand side of Equation 2.6 contains temporal and spatial heat exchange. Terms in the first bracket arise from the heat and turbulent flow. Equation contains the source term of specific enthalpy, exchange of energy due to mass and surface forces, the temporal change of pressure of the particular phase together with the energy exchange between phases.

## 2.4. Turbulence modelling

One classification of the flow type is laminar (stable, arranged) and turbulent (chaotic) flow. For the most cases in engineering applications, the flows are turbulent. That is the reason that the RANS (Reynolds Averaged Navier-Stokes) is used to describe the nature of turbulent flows. RANS enable rather quick, yet satisfactory solution to turbulent flows in various engineering applications. With RANS approach, instant values of the turbulent flow are replaced with the averaged values and their corresponding oscillations. Regarding that, two new terms are introduced to the conservation laws: Reynolds stress tensor and the turbulent heat flux. For the purpose of this thesis, the  $k-\zeta-f$  turbulence model was used.

### 2.4.1. $k-\zeta-f$ turbulence model

$k-\zeta-f$  model is based on the Durbin's concept of elliptical relaxation, respectively additional transport equation for velocity ratio is solved  $\zeta = \bar{v}^2$ . Model is suitable for spray process calculation and for the swirling motion description, which is a characteristic of the internal combustion engines [29].

$$\nu_t = C_\mu \zeta \frac{k^2}{\varepsilon} \tag{2.7}$$

In Equation 2.7,  $C_\mu$  is the model constant,  $k$  is the turbulent kinetic energy,  $\varepsilon$  is the turbulent kinetic energy dissipation rate and  $\zeta$  is the velocity scale ratio. Other variables are determined according to:

$$\begin{aligned}\rho \frac{Dk}{Dt} &= \rho (P_k - \varepsilon) + \frac{\partial}{\partial x_j} \left[ \left( \mu \frac{\mu_t}{\sigma_k} \right) \frac{\partial k}{\partial x_j} \right], \\ \rho \frac{D\varepsilon}{Dt} &= \rho \frac{C_{\varepsilon 1}^* P_k - C_{\varepsilon 2} \varepsilon}{T} + \frac{\partial}{\partial x_j} \left[ \left( \mu \frac{\mu_t}{\sigma_k} \right) \frac{\partial \varepsilon}{\partial x_j} \right], \\ \rho \frac{D\zeta}{Dt} &= \rho f - \rho \frac{\zeta}{k} P_k + \frac{\partial}{\partial x_j} \left[ \left( \mu \frac{\mu_t}{\sigma_k} \right) \frac{\partial \zeta}{\partial x_j} \right].\end{aligned}\tag{2.8}$$

Elliptic function  $f$  is calculated as:

$$f - \frac{\partial^2 f}{\partial x_i \partial x_j} L^2 = \left( C_1 + C_2 \frac{P_k}{\zeta} \right) \frac{\frac{2}{3} - \zeta}{T}.\tag{2.9}$$

where the turbulent length  $L$  and turbulent time  $t_t$ , are derived from Equation 2.10.

$$\begin{aligned}L &= C_L \max \left[ \min \left( \frac{k^{1.5}}{\varepsilon}, \frac{k^{0.5}}{\sqrt{6} C_\mu |S| \zeta} \right), C_\eta \left( \frac{\nu^3}{\varepsilon} \right)^{0.25} \right], \\ t_t &= \max \left[ \min \left( \frac{k}{\varepsilon}, \frac{0.6}{\sqrt{6} C_\mu |S| \zeta} \right), C_T \left( \frac{\nu}{\varepsilon} \right)^{0.5} \right].\end{aligned}\tag{2.10}$$

## 2.5. Mass transfer modelling

In order to model the central phenomena of the thesis - fuel evaporation process, a transfer of properties among the phases needs to be modelled as well. Therefore, to describe a mass exchange between the continuous phase (liquid fuel) and dispersion phase (gaseous fuel), the Non-Linear Cavitation Model was set. The flash boiling operating conditions were modelled with the Flash Boiling Model.

### 2.5.1. Non-Linear Cavitation Model

The change of mass inside of the Non-Linear Cavitation model is based on the Equation 2.11, where  $N'''$  describes bubble number density, and  $R$  represents the bubble radius, while the temporal derivative of  $R$  is marked with  $\dot{R}$  [4]. Subscripts  $c$  and  $d$  refer to the

continuous and dispersed phase.

$$\Gamma_c = \rho_d N''' 4\pi R^2 \dot{R} = -\Gamma_d \quad (2.11)$$

Bubble radius is defined through the volume fraction  $\alpha_d$  and the bubble number density  $N'''$ , from which follows the definition for the radius:

$$R = \left( \frac{3\alpha_d}{4\pi N'''} \right)^{1/3}. \quad (2.12)$$

Temporal derivative of the bubble radius, given with the Equation 2.14, is obtained from Rayleigh equation:

$$R\ddot{R} + \frac{3}{2}\dot{R}^2 = \frac{\Delta p}{\rho_c}. \quad (2.13)$$

$$|\dot{R}| = \sqrt{\frac{2}{3} \frac{|\Delta p|}{\rho_c} - R\ddot{R}} \quad (2.14)$$

Effective pressure difference  $\Delta p$ , given with the Equation 2.15, includes the fluctuation effects resulting from the pressure actuation. Egler coefficient of closure  $C_E$  depends on the local turbulence level, and considering the type of the application,  $C_E$  is taken from the range defined by Equation 2.16.

$$\Delta p = p_{sat} - \left( p - C_E \frac{2}{3} \rho_c k_c \right), \quad (2.15)$$

$$C_E = 0.3 \sim 1.4. \quad (2.16)$$

The mass exchange equation is derived:

$$\Gamma_c = -\Gamma_d = \begin{cases} C_e \rho_d \left( 3\alpha_d^{2/3} (4\pi N''')^{1/3} \right) |\dot{R}| & \Delta p \geq 0 \\ -\frac{1}{C_r} \rho_d (3\alpha_d)^{2/3} (4\pi N''')^{1/3} |\dot{R}| & \Delta p < 0 \end{cases} \quad (2.17)$$

In the equation above, coefficients  $C_e$  and  $C_r$  are empirical coefficients which regulate the increase and reduction of the vaporization during the condensation process.  $C_e$  and  $C_r$  are introduced to account for discrepancies between the simulation and observed behaviour of the fluids. In the ideal case, their value equals to unity [4].

### 2.5.2. Flash Boiling model

The primary control factor of the flash boiling model is the degree of superheat  $\Delta T_{sup}$ , given by Equation 2.18:

$$\Delta T_{sup} = T_c - T_{sat}, \quad (2.18)$$

where  $T_c$  represents superheated liquid temperature in the flow field, and  $T_{sat}$  is the saturated vapour temperature of liquid at given pressure condition. The advanced Hertz-Knudsen correlation is given with the following equation [30]:

$$\dot{R} \times A''' = (3\alpha_d)^{\frac{3}{2}} (4\pi N''')^{\frac{1}{3}} \frac{p_{sat} - p}{\sqrt{2\pi R_g T_{int}}}. \quad (2.19)$$

In Equation 2.19,  $A'''$  is the bubble surface area, and  $N'''$  is the bubble number density. The gas constant is labelled with  $R_g$ , while  $p_{sat}$  and  $T_{sat}$  are representing the saturation pressure and the bubble interface temperature. Temperature  $T_{sat}$  is obtained from:

$$T_{int} = \frac{\alpha_c \rho_c C_{P_c} T_c + \alpha_d \rho_d C_{P_d} T_d}{\alpha_c \rho_c C_{P_c} + \alpha_d \rho_d C_{P_d}}, \quad (2.20)$$

where  $T_{int}$  represents the initial temperature, and indices  $c$  and  $d$  correspond to the continuous and dispersed phase. The bubble number density is determined from the following equation [31]:

$$N''' = N_0''' \times \exp\left(\frac{-5.279}{\Delta T_{sup}}\right), \quad (2.21)$$

where the initial bubble number density is labelled with  $N_0'''$ . Thereby, the flash boiling model can be expressed in two variants:

- with the constant number density, or
- with the number density defined as a function of superheat degree.

Hence, the mass interfacial exchange is given by Equation 2.22 where  $\lambda_{ac}$  represents the accommodation factor.

$$\Gamma_c = -\Gamma_d = \begin{cases} \lambda_{ac} C_e A''' |\dot{R}| & (p_{sat} - p) \geq 0 \\ -\frac{\lambda_{ac}}{C_r} A''' |\dot{R}| & (p_{sat} - p) < 0 \end{cases} \quad (2.22)$$

## 2.6. Momentum transfer modelling

Momentum exchange at the interface between the liquid and gaseous fuel is described with the Cavitation Drag model. Moreover, the Gas-Liquid 3 [4] model describes the transfer of momentum between the surrounding nitrogen and the liquid fuel.

### 2.6.1. Cavitation Drag Model

Interfacial momentum exchange includes drag forces and turbulent dispersion forces, according to the expression:

$$\mathbf{M}_c = C_D \frac{1}{8} \rho_c A_i''' |\mathbf{v}_r| \mathbf{v}_r + C_{TD} \rho_c k_c \nabla \alpha_d + \mathbf{F}_L + \mathbf{F}_{WL} = -\mathbf{M}_d, \quad (2.23)$$

where the relative velocity is defined as:

$$\mathbf{v}_r = \mathbf{v}_d - \mathbf{v}_c. \quad (2.24)$$

Drag coefficient for the bubbles is a relation of Reynolds number  $\text{Re}$ :

$$C_D = \begin{cases} \frac{192}{\text{Re}_b} (1 + 0.10 \text{Re}_b) & \text{Re}_b \leq 1000 \\ 0.438 & \text{Re}_b > 1000 \end{cases} \quad (2.25)$$

Reynolds number used in 2.25 reads as:

$$\text{Re}_b = \frac{|v_r| D_b}{\nu_c}. \quad (2.26)$$

Turbulent dispersion coefficient  $C_{TD}$  describes the diffusion of vapour due to turbulence. The bubbles or droplets contact area density is obtained using the following expression:

$$A_i''' = \pi D_d^2 N''' = (36\pi)^{1/3} N'''^{1/3} \alpha_d^{2/3} = \frac{6\alpha_d}{D_d}, \quad (2.27)$$

where the diameter of the dispersion phase (bubble or droplet) is marked with  $D_d$ , while  $\alpha_d$  represents the volume fraction of the vapour phase. Terms  $\mathbf{F}_L$  and  $\mathbf{F}_{WL}$  represents lift and wall lubrications forces.

### 2.6.2. Gas Liquid System 3

According to [32], Gas Liquid System 3 model states: When value of  $\alpha_2$  is lower than the critical bubbly flow volume fraction, the drag force is established from the bubbly drag coefficient  $C_D^{bub}$ , and in the case where the value of  $\alpha_2$  is greater than the critical droplet flow volume fraction, the drag force is calculated from droplet drag coefficient  $C_D^{drpl}$ . When the value of  $\alpha_2$  is between critical bubbly and droplet volume fractions, the drag force is determined by combining the bubbly and droplet drag. Therefore, the momentum interphase exchange within this model is calculated from Equation 2.23 used in the Cavitation Drag Model. Since the dispersion coefficient value is set to zero, the final form of Equation 2.23 becomes:

$$\mathbf{M}_c = C_D \frac{1}{8} \rho_c A_i''' |\mathbf{V}_r| \mathbf{V}_r + \mathbf{F}_L + \mathbf{F}_{WL} = -\mathbf{M}_d. \quad (2.28)$$

## 2.7. Enthalpy transfer modelling

Enthalpy exchange at the liquid and gaseous fuel interface is described with Ranz-Marshall 2 model.

### 2.7.1. Ranz-Marshall 2

The Ranz-Marshall heat exchange is based on the Ranz-Marshall correlation for the Nusselt number  $Nu$  obtained from the dispersed phase:

$$Nu = 2 + 0.6 Re_b^{\frac{1}{2}} Pr^{\frac{1}{3}}. \quad (2.29)$$

In the equation above,  $Re_b$  is the local bubble Reynolds number and  $Pr$  is the Prandtl number. The following equation describes the heat transfer rate:

$$H_c = C_H \frac{\kappa_c}{D_b} Nu A_i''' (T_d - T_c) = -H_d, \quad (2.30)$$

where  $C_H$  represents the model constant which considers the deviation from spherical droplet/bubble shape.  $\kappa_c$  is the continuous phase conductivity, taken from the gas phase in this model. The dispersed phase diameter is given with the term  $D_d$ , while  $A_i'''$



represents the interfacial area density defined with Equation 2.31.

$$A_i''' = \frac{6\alpha_d}{D_d} \quad (2.31)$$

The dispersed phase is in that case determined by the following criterion:

$$\alpha_d = \begin{cases} \alpha_2, & \alpha_2 \leq 0.5 \\ \alpha_1, & \alpha_2 > 0.5 \end{cases}. \quad (2.32)$$

# 3 Computational mesh and numerical setup

Numerical simulations were carried out in a commercial 3D CFD software AVL FIRE<sup>TM</sup>. Two different operating conditions for ECN GDI injector were investigated. The first, referred to as Spray G, represents the standard operating conditions. The second, denoted as Spray G2, contains flash boiling conditions inside the discharge volume. Within this chapter, the ECN GDI injector geometry, as well as the related computational mesh are described. Furthermore, the corresponding boundary and initial conditions are given in Section 3.2.. The description of Nozzle file configuration is given in Section 3.3., and finally, in Section 3.4. the simulation numerical setup is outlined.

## 3.1. Structured computational mesh

Three generations of GDI injector geometry were available from [5]. In this work, the third generation direct fuel injector was used, which was obtained by the experimental measuring and corresponds to a real injector geometry with high accuracy. The injector geometry can be observed in Figure 3.1.

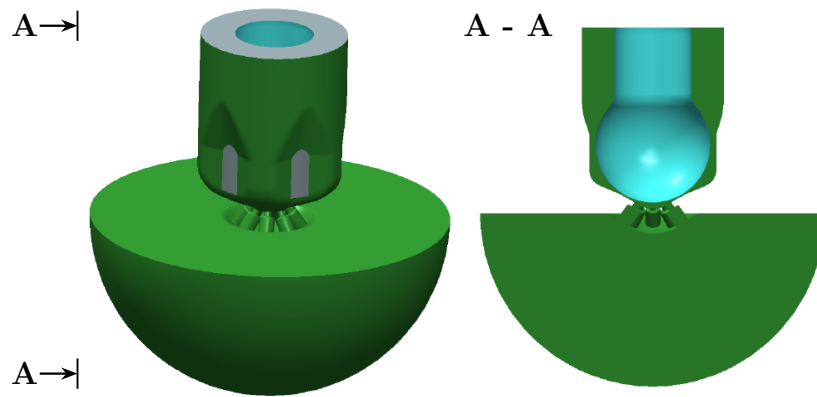


Figure 3.1: GDI injector surface [5]

The structured computational mesh was generated according to the injector surface provided from ECN. Injector computational domain, shown in Figures 3.2 and 3.3, contains 1 233 920 hexahedral cells and can be roughly divided into three main parts: needle, nozzle holes and discharge volume, which are further used for creating the required selections.

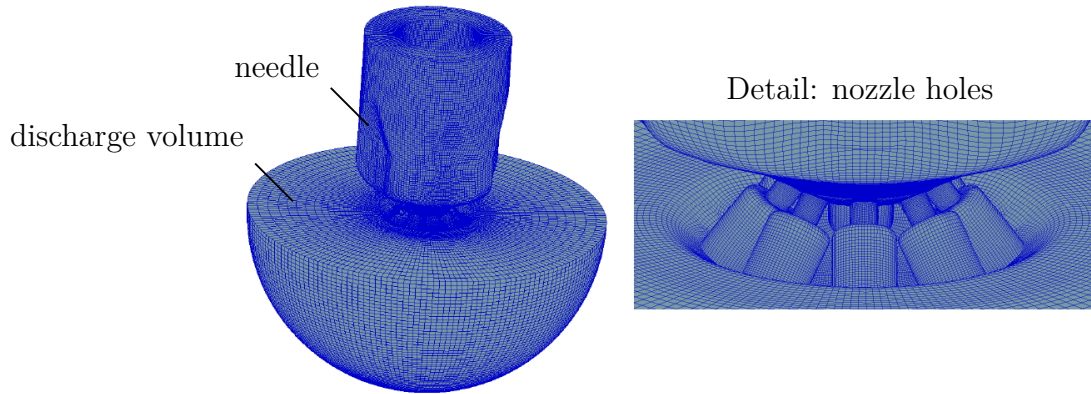


Figure 3.2: GDI injector computational mesh

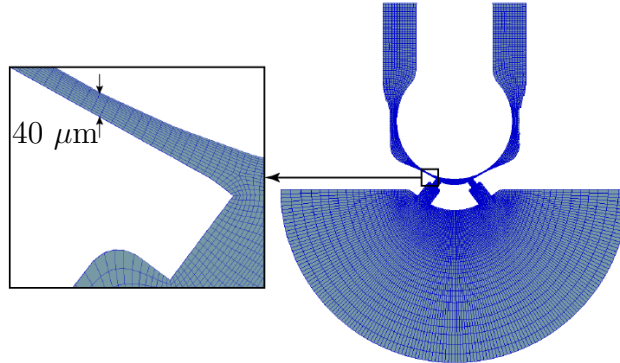


Figure 3.3: Details of GDI injector computational mesh

The initial injector mesh was created as a non moving domain with the needle lift of  $40\ \mu\text{m}$ , as displayed in Figure 3.3. In order to simulate the injection process, the needle motion needed to be taken into consideration. For that purpose, appropriate selections, displayed in Figure 3.4a), were created. At the beginning of the injection process, the needle had to be placed in the closed position. Before realization of moving computational mesh, several changes regarding the mesh fineness were done. Since the buffer selection was meshed in “one piece”, meaning that mesh refinement contains the exact number of divisions across the entire cross-section, problem with the mesh movement

occurred. Complication originated at the narrowest part of geometry, i.e. in the space between the needle and injector body, represented in Figure 3.3. Due to the vertical needle movement (-Y axis), and owing to a large number of cells, an overlap occurred and consequently, negative volumes on the computational domain appeared. Thus, the mesh refinement was performed by means of reducing the number of distributions along the buffer cross-section, as shown in Figure 3.4b). The number of elements was therefore reduced to 1 112 576 hexahedral cells.

The mesh deformation was defined by a formula. First, a mesh deformation was performed with the aim of descending the needle to the closed position. To maintain the numerical stability, it was not possible to completely close the needle. Therefore, when referring to the initial position in the simulations, a gap of  $6\ \mu\text{m}$  exists at the narrowest needle seat region.

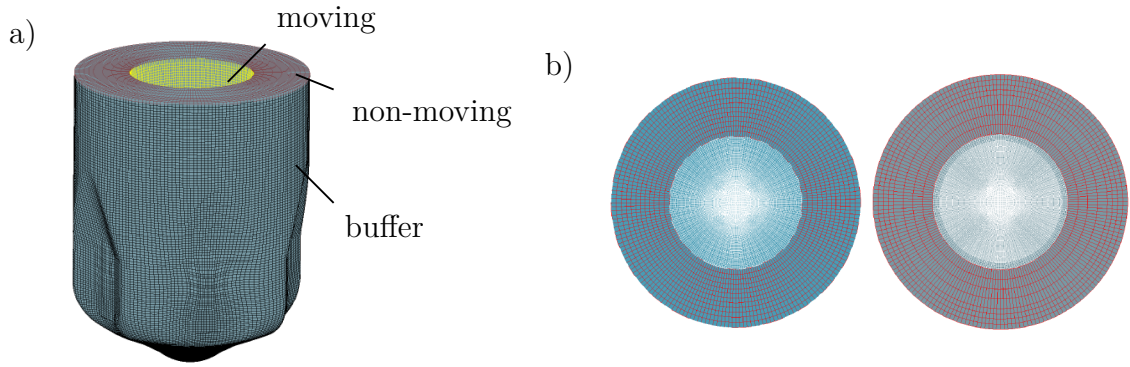


Figure 3.4: a) Selections for mesh movement, b) mesh refinement

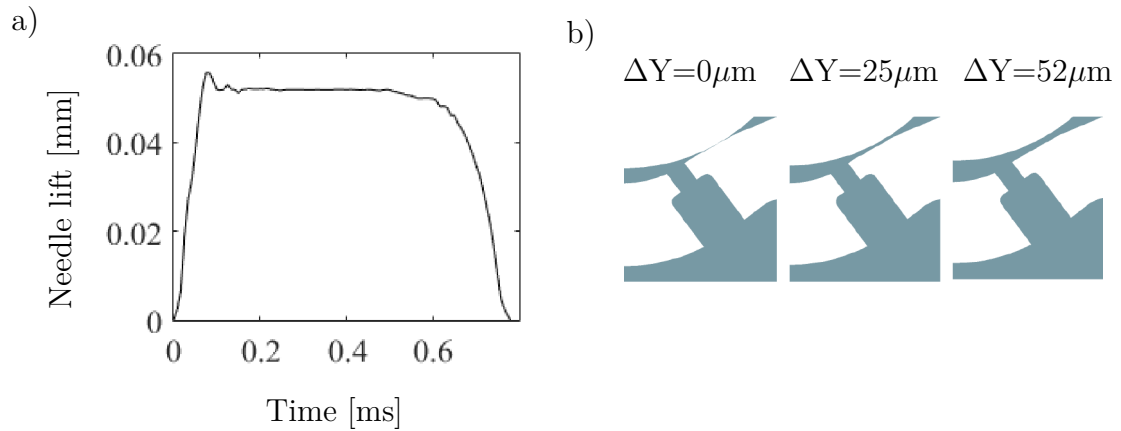


Figure 3.5: a) Needle lift curve, b) needle positions for  $\Delta Y=0\ \mu\text{m}$ ,  $\Delta Y=25\ \mu\text{m}$  and  $\Delta Y=54\ \mu\text{m}$

After the needle had been settled in the desired position, the mesh was further used as the initial injector computational domain. Finally, realistic injector movement was achieved by lifting and descending the injector needle in accordance with the curve taken from [6]. Lifting curve and different needle positions are shown in Figure 3.5.

## 3.2. Boundary and initial conditions

Boundary and initial conditions were set throughout the corresponding selections created on the computational domain. As previously stated, an interaction between the plumes was found according to [26] and [8], which is why the complete injector geometry should be considered. The boundary conditions used to simulate the Spray G injector were defined through face selections displayed in Figure 3.6:

- inlet boundary (defined with *inlet* selection)
- outflow boundary (defined with *outlet* selection)
- wall boundary (defined with *wall* and *needle* selections)

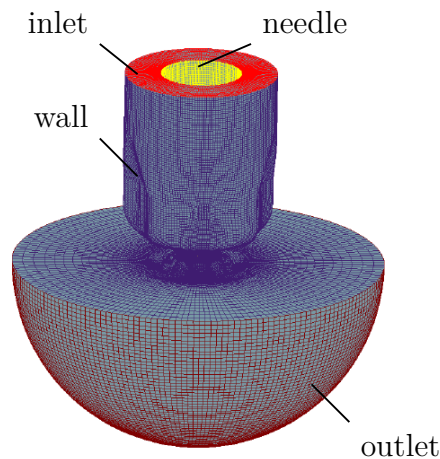


Figure 3.6: Selections for boundary conditions

The in-nozzle flow was modelled using the Eulerian multiphase approach, implemented in the AVL FIRE<sup>TM</sup> code. This model enables definition of an arbitrary number of phases, with each having a unique velocity and turbulence solution, while the pressure solution is shared among the phases. Since the primary focus of this thesis is investigation of the fuel evaporation, the fuel injection process was also modelled with the

Eulerian multiphase model. Therefore, all boundary conditions needed to be defined for all phases. Defined fluid properties are given in Table 3.1.

Table 3.1: Fluid properties

<b>Phase 1: ISO-OCTANE</b>	
Diffusion coefficient [-]	0.0257
Reference pressure [Pa]	100 000
Reference temperature [K]	363
Turbulent Schmidt No.	0.9
<b>Phase 2: Gaseous fuel</b>	
Density [kg/m <sup>3</sup> ]	1.1
Dynamic viscosity [Ns/m <sup>2</sup> ]	1.824e-5
<b>Phase 3: Nitrogen</b>	
Density [kg/m <sup>3</sup> ]	3.5 (G) / 0.5 (G2)
Dynamic viscosity [Ns/m <sup>2</sup> ]	1.824e-5

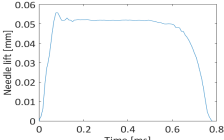
The inlet boundary condition was defined through the injection pressure of 200 bar, the temperature inside the injector of 363 K, turbulence kinetic energy (TKE) of 0.1 m<sup>2</sup>/s<sup>3</sup> and turbulence length scale (TLS) of 0.001 m. Also, volume fractions of each phase were set: the volume fraction of liquid fuel was set with the value of 0.999998, while the volume fractions of gaseous fuel and nitrogen inside the injector are equal to 1e-6. Theoretically, the injector is completely filled with liquid fuel, but due to requirements of the employed approach, a positive value for all defined phases needed to be set.

Outlet boundary condition, as well as the Inlet condition, were defined by setting the pressure shared by all phases. In case of standard Spray G operating conditions, a pressure inside the discharge volume equals 6 bar, while in case of flash boiling condition, pressure inside the combustion chamber is equal to 0.5 bar, below the atmospheric pressure. The discharge volume was filled with nitrogen. Therefore, volume fractions of liquid and gaseous fuel were set to 1e-6, while the volume fraction of nitrogen equals 0.999998.

The injector wall was defined with a thermal boundary condition by setting the temperature of 363 K.

The temperature of the needle boundary condition, which was also defined as an impermeable wall, was set as 363 K. All boundary conditions are summarized in the Table 3.2.

Table 3.2: Boundary conditions

	Phase 1	Phase 2	Phase 3
Inlet			
Pressure [bar]	200	-	-
Volume fraction [-]	0.999998	1e-6	1e-6
Temperature [K]	363		
TKE [m <sup>2</sup> /s <sup>3</sup> ]	0.1		
TLS [m]	0.001		
Outlet			
Pressure [bar]	6 (G) / 0.5 (G2)	-	-
Volume fraction [-]	1e-6	1e-6	0.999998
Wall			
Thermal	Temperature, 363 [K]		
Needle			
Thermal	Temperature, 363 [K]		
Movement	Mesh movement (needle lift curve)		
			

Initial conditions were defined through cell selections created on the computational mesh. The liquid initial condition prescribes pressure of 200 bar, temperature of 363 K, turbulence kinetic energy of  $0.1 \text{ m}^2/\text{s}^3$  and turbulence length scale of 0.001 m. Volume fractions of all phases were set as well, and for the liquid fuel, that amount equals 0.999998, while the volume fractions of gaseous fuel and nitrogen were set with the value of 1e-6. It can be noticed that liquid initial conditions correspond to the boundary conditions set on the inlet selection.

The second type of initial conditions, nitrogen initial conditions, determine the state of ambient gas in a specified area of computational domain. With the combination of initial conditions, a desired initialization position of a particular phase is achievable. Assigning the nitrogen initial conditions to the selections, as shown in Figure 3.7, liquid fuel was initialized up to the needle seat area. Therefore, for the standard simulation, the pressure value of 6 bar and temperature of 573 K were set, while for the flash boiling case these values were 0.5 bar and 333 K. With the volume fractions, the nitrogen with the value of 0.999998, was set as a dominant phase within selection for which the condition was set. Traces of liquid and gaseous fuel were set with the volume fractions of 1e-6. Turbulence kinetic energy and turbulence length scale values for both simulations equals  $0.1 \text{ m}^2/\text{s}^3$  and  $5\text{e-}5 \text{ m}$ .

Initialization methodology for standard and flash boiling simulations is shown in Figure 3.8. Numerical setup of general and initial conditions, for standard Spray G and flash boiling Spray G2 conditions, is given in Table 3.3.

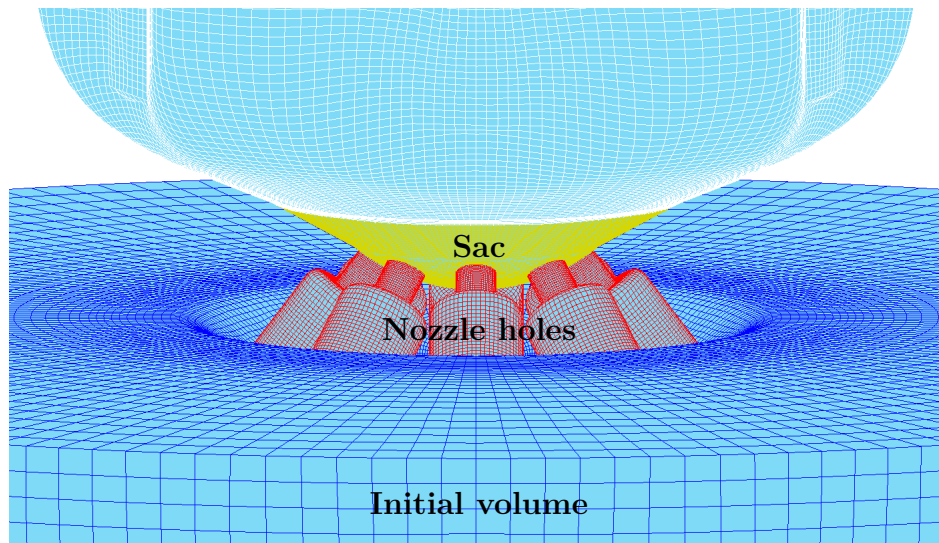


Figure 3.7: Selections for nitrogen initial conditions



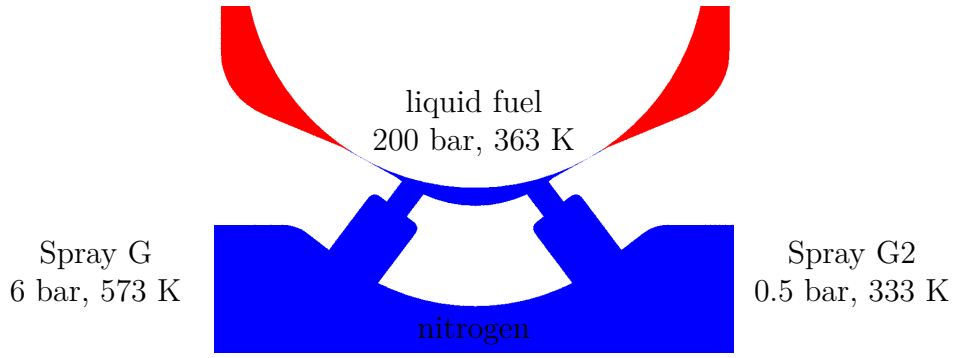


Figure 3.8: Initialization methodology

Table 3.3: Initial conditions

Liquid initial conditions			
	Phase 1	Phase 2	Phase 3
Pressure [bar]	200	-	-
Volume fraction [-]	0.999998	1e-6	1e-6
Temperature [K]	363		
TKE [m <sup>2</sup> /s <sup>3</sup> ]	0.1		
TLS [m]	0.001		
Initialization mode	Uniform		
Nitrogen initial conditions:			
Initial volume, Nozzle holes, Sac			
Pressure [bar]	6 (G) / 0.5 (G2)	-	-
Volume fraction [-]	1e-6	1e-6	0.999998
Temperature [K]	573 (G) / 333 (G2)		
TKE [m <sup>2</sup> /s <sup>3</sup> ]	0.1		
TLS [m]	5e-5		
Initialization mode	Uniform		

### 3.3. *Nozzle file* configuration

*Nozzle file* is an ASCII file with the \*.nzf extension, where the flow data are written during the simulation [4]. File has a flexible structure that depends on the number of phases used in the simulation, number of elements contained in the observed selection,

etc. *Nozzle file* structure is divided by a header, where the information regarding the number of surface elements, number of used phases, nozzle properties, number of written data, etc. is saved, and body. Geometry and flow data are registered in the body of *Nozzle file* grouped into blocks. *Nozzle file* structure is given in Table 3.4.

In the first row, terms  $t$  and  $n$  represent a time step for which the data in the block are written and a number of elements for which the file is generated. In the second row, with  $m_1$ ,  $m_2$  and  $m_3$ , values of a mass flow for the respective phase are given. Right after, the geometrical characteristics of each element are described. Specifically,  $x_{cen}$ ,  $y_{cen}$  and  $z_{cen}$  are the element centre coordinates, with  $f$ , the element area is marked, and the components of element vector normal are given with  $x_{nor}$ ,  $y_{nor}$  and  $z_{nor}$ . Velocity components of each phase are given with the terms  $u$ ,  $v$ , and  $w$ , while  $k$  and  $\varepsilon$  represent turbulent kinetic energy and turbulence dissipation rate. Phase density is marked with  $\rho$ , and phase temperature with  $T$ . Flow attributes of all phases are written with terms  $S_1$  and  $S_2$ , in the last row of a block [4].

Table 3.4: *Nozzle file* structure

$t$	$n$						
$m_1$	$m_2$	$m_3$					
$x_{cen}$	$y_{cen}$	$z_{cen}$	$f$	$x_{nor}$	$y_{nor}$	$z_{nor}$	
$u$	$v$	$w$	$k$	$\varepsilon$	$\rho$	$\alpha$	$T$
$S_1$	$S_2$						

As it was already mentioned, one *Nozzle file* can be set for one face selection on the computational domain. Since the injector examined in this work has eight nozzle holes, eight selections for *Nozzle file* generation were created. These selections comprise every nozzle hole outlet cross-section or, to be more precise, counterbores outlet cross-section. With the bottom view of injector body in Figure 3.9, the selections used for *Nozzle file* generation are shown. Nozzles are labelled clockwise with capital letters A - H.

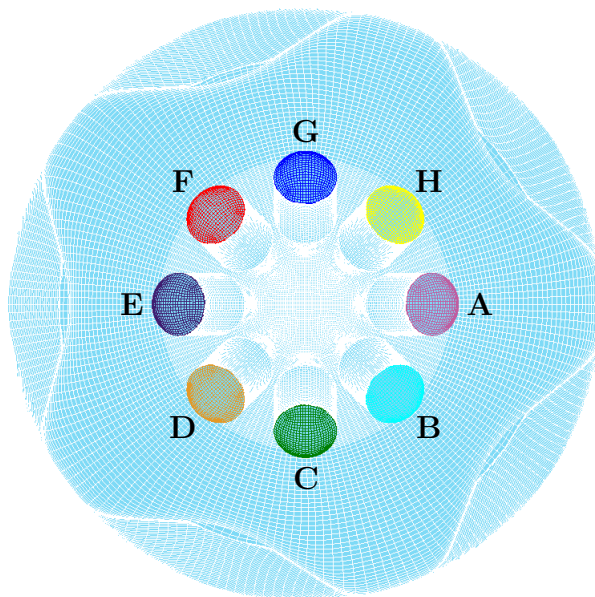


Figure 3.9: Selections for *Nozzle file* generation

Considering the great amount of saved information, *Nozzle file* was post-processed with MATLAB, where the script that improves accessibility and readability of flow data was created. Thus, in a very short time, arbitrary flow data for any element in any timestep can be reached. MATLAB script is enclosed in Appendix.

### 3.4. Numerical simulation setup

Transient, viscous, and turbulent flow has been observed. It is possible to set the numerical integration step in two ways: by setting a crank-angle or time step. Since the data for needle lift curve were given in mm per second, time step run mode was chosen. Duration of simulation was defined with the end time of  $780 \mu\text{s}$ , and the size of a time step was set to automatic with its minimum value of  $1\text{e-}10$  s. In that case, the Courant-Friedrichs-Lewy (CFL) condition for liquid phase analysis was activated and set with the value of 3. CFL condition is used for the stability of the unstable numerical methods that model convection or wave phenomena. It defines that a distance any information travels during the time step length within the mesh must be lower than the distance between the mesh elements. In other words, information from a given cell or mesh element must propagate only to its immediate neighbours [33]. Maximum time step size was set to  $5\text{e-}8$  s. Moreover, a multiphase module was activated, within which

three phases, described in Table 3.1, were defined.

For solving the momentum, turbulence and energy conservation equations, together with the compatibility equation, the combination of Central Differencing Scheme (CDS) and Upwind Differencing Scheme (UDS) with a blending factor of 0.5 was used. The solution of the continuity equation was calculated by CDS. Underrelaxation factors  $\chi$ , are defined to prevent the solution from diverging. Working principle of iterative methods lies in taking the part of previous iteration solution of observed variable  $\varphi^{old}$ , and adding it to a current iteration solution  $\varphi^{new}$ , described with the expression 3.1. Therefore, with the underrelaxation factors, given in Table 3.5, the amount of the previous solution entering the calculation is set. Values of underrelaxation factors are within the range from 0 - 1, and the lower the value, numerical simulation is more stable, but concurrently, the duration of the simulation is increased.

$$\varphi = \varphi^{old} + \chi (\varphi^{new} - \varphi^{old}) \quad (3.1)$$

Table 3.5: Underrelaxation factors

	Spray G	Spray G2
Pressure	0.15	0.15
Momentum	0.3	0.3
TKE	0.4	0.4
TDS	0.4	0.4
Energy	0.6	0.8
Scalar	0.8	0.8
Volume fraction	0.85	0.8

Solving the non-linear partial differential equations comes down to iterative solving of the linearised system of equations until the solution reaches desired accuracy. Therefore, after the normalized residuals falls below the set value, a numerical procedure is stopped. The convergence criteria for both performed calculations are given in Table 3.6.

Table 3.6: Convergence criteria

	Spray G / Spray G2
Maximum number of iterations	80
Minimum number of iterations	3
Pressure	0.001
Momentum	0.001
TKE	0.005
TDS	0.005
Volume fraction	0.005

The main difference in the numerical setup of standard Spray G and flash boiling case is in the interfacial properties exchange. Therefore, to describe the fuel evaporation process, the mass interfacial exchange in the standard simulation is set with the Non-Linear Cavitation Model, while in the flash boiling condition setup, Flash Boiling Model was employed.

For the momentum exchange, three interfaces were activated. First, two-fluid Cavitation Drag model was set for the exchange of momentum between the liquid (phase 1) and gaseous (phase 2) fuel phase. Momentum exchange among nitrogen (phase 3) and the liquid fuel was defined with the Gas-Liquid3 model. Finally, homogeneous exchange of momentum is set with the General model between phases 3 and 2.

Enthalpy interface exchange in case of flash boiling operating conditions was defined with the General model [4] for phases 3 and 2, and Two-fluid Ranz-Marshall 2 model was used for exchanging the enthalpy among liquid and gaseous fuel. For the standard Spray G simulation, enthalpy interface exchange was not utilized.

The exchange of turbulence in both simulations, between the nitrogen and gaseous fuel, was set as general.

## 4 Results

Calculations of Spray G, under the standard and flash boiling operating conditions, are carried out. The results of simulations described in the previous Chapter 3. are tested against experimental data. First, results are given in a form of a diagrams, where the represented data are taken from *Nozzle files* generated for each nozzle. During the nozzle flow simulation, data describing the flow process at the nozzle outlet cross-section are written in ASCII file with \*.nzf extension. Secondly, a 3D results processed within AVL FIRE<sup>TM</sup>, for Spray G and G2, are represented and discussed. Finally, the computed and experimental data are compared.

Figures 4.1 and 4.2 show the mass flow rate of liquid phase during the whole injection process under the standard operating conditions. Comparing the total mass flow rate curves in Figure 4.1, the difference between simulation and experiment is obvious. However, both curves show a similar behaviour. Moreover, the deviation between the mass flow curves is constant through the whole fuel injection process. That behaviour can be attributed to simplification of needle motion and domain geometry. In other words, only vertical needle movement is considered when performing a simulation, while wobbling in X and Y axis is neglected. In the experiment, in a closed needle position there is no gap at the needle seat, while in the simulations, a gap of 6  $\mu\text{m}$  between the needle and injector wall was considered. Although the numerical needle movement was shaped according to experimentally obtained curve, the size of that gap results with a small increase in mass flow rate. Figure 4.2 shows the mass flow rate for each nozzle where data are recorded at the counterbore outlet. It can be seen that curves follow a similar profile with individual oscillations. As it is explained earlier, a number of factors, such as nozzle holes geometry, manufacturing imperfections, horizontal needle movement, etc., impact the flow.

In the same way, data from the flash-boiling simulation are collected, processed, and represented in Figures 4.3 and 4.4. Due to the larger pressure difference, Spray G2 flow reaches higher values when compared to the standard condition. However, the injection curve follows a standard injection trend. Liquid disintegration, noticed around  $600 \mu\text{s}$ , is attributed to the start of needle descending. It is found in [7] that at the low needle position the flow fluctuations may occur. Presence of hole-to-hole variations is shown in Figure 4.4.

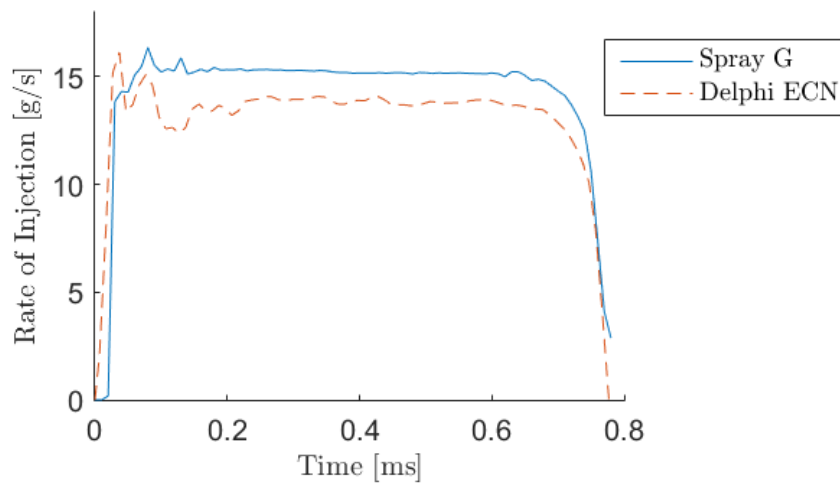


Figure 4.1: Total mass flow rate of standard Spray G calculation compared with experimental results

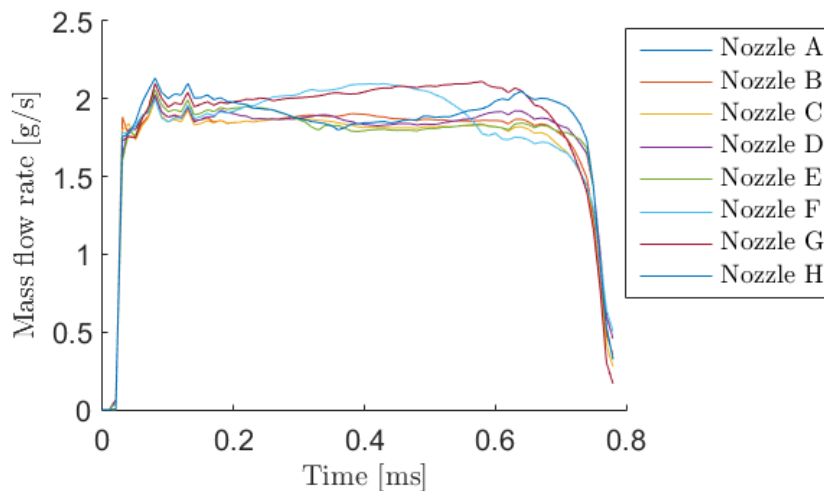


Figure 4.2: Mass flow rate of each nozzle for standard Spray G calculation

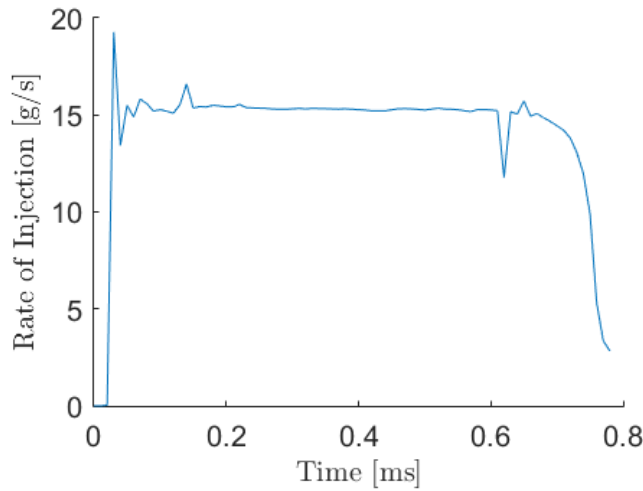


Figure 4.3: Total mass flow rate of Spray G flash boiling calculation

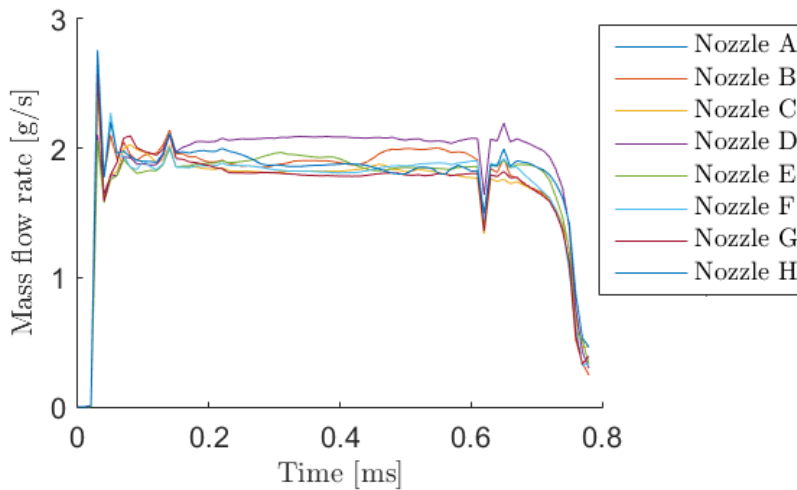


Figure 4.4: Mass flow rate of each nozzle for Spray G flash boiling calculation

The area below the mass flow rate curves represents the mass of injected liquid fuel. Hence, by integrating the individual nozzle injection profiles, mass of injected fuel per nozzle is calculated. The result is qualitatively given in the chart shown in Figure 4.5, where hole-to-hole variation between the two simulations is compared. Spray G is showing a more balanced mass distribution than Spray G2. Therefore, the total mass of injected fuel in the experiment equals 10.16 mg, while in the cases of numerical simulation fuel mass equal to 11.08 mg in standard spray condition, and 11.12 mg for the flash-boiling case.



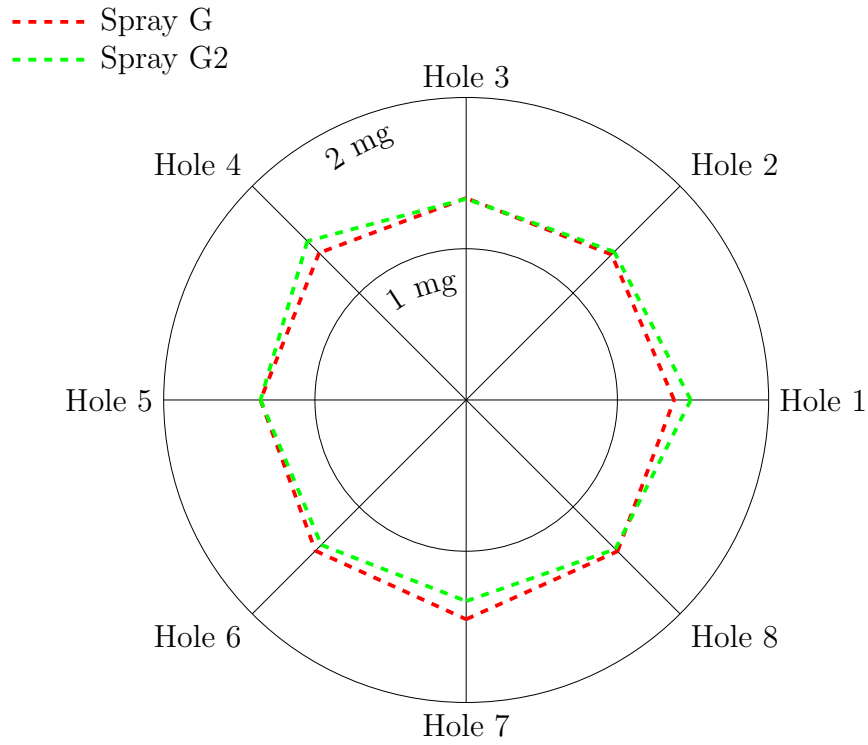


Figure 4.5: Injected mass: hole-to-hole variation

Table 4.1: Hole-to-hole variation in mass flow and according discharge coefficients

Hole	Mass flow [%]		C <sub>d</sub>		Mass flow [%]		C <sub>d</sub>	
	AVL FIRE™				OpenFOAM [8]			
	G	G2	G	G2	G	G2	G	G2
1	12.1	13.9	0.47	0.55	12.5	12.4	0.53	0.52
2	12.3	13.3	0.48	0.54	12.2	12.0	0.52	0.50
3	12.0	12.1	0.47	0.48	12.7	13.1	0.54	0.55
4	11.9	12.3	0.47	0.50	13.0	12.3	0.55	0.52
5	12.0	12.3	0.47	0.50	12.9	12.4	0.55	0.52
6	13.5	12.4	0.52	0.50	11.9	12.0	0.51	0.50
7	13.8	11.9	0.53	0.48	12.1	12.7	0.51	0.53
8	12.5	12.0	0.49	0.48	12.7	13.1	0.54	0.55

The mass flow through each nozzle hole and the associated discharge coefficients, for both G and G2 simulations carried out in AVL FIRE<sup>TM</sup>, are further compared to numerical analyses performed in OpenFOAM by [8]. The results are given in the Table 4.1. The mass flow is given by percentage, in reference to the total mass flow. Discharge coefficients are calculated by the expressions according to [34]. Simulations in OpenFOAM were carried out on the fixed computational domain with the needle placed in the most opened position, which explains higher discharge coefficients than in cases concerned in this thesis. With respect to the ideal mass flow fraction of 12.5%, a slight deviation is noticed.

Furthermore, 3D results of performed simulations are presented. In Figure 4.6, the liquid phase volume fraction at the early stage of injection for the standard case is displayed. Due to the large flow turning angle, i.e. sharp nozzle inlet edge, when the flow enters the nozzle, liquid flow separation occurs.

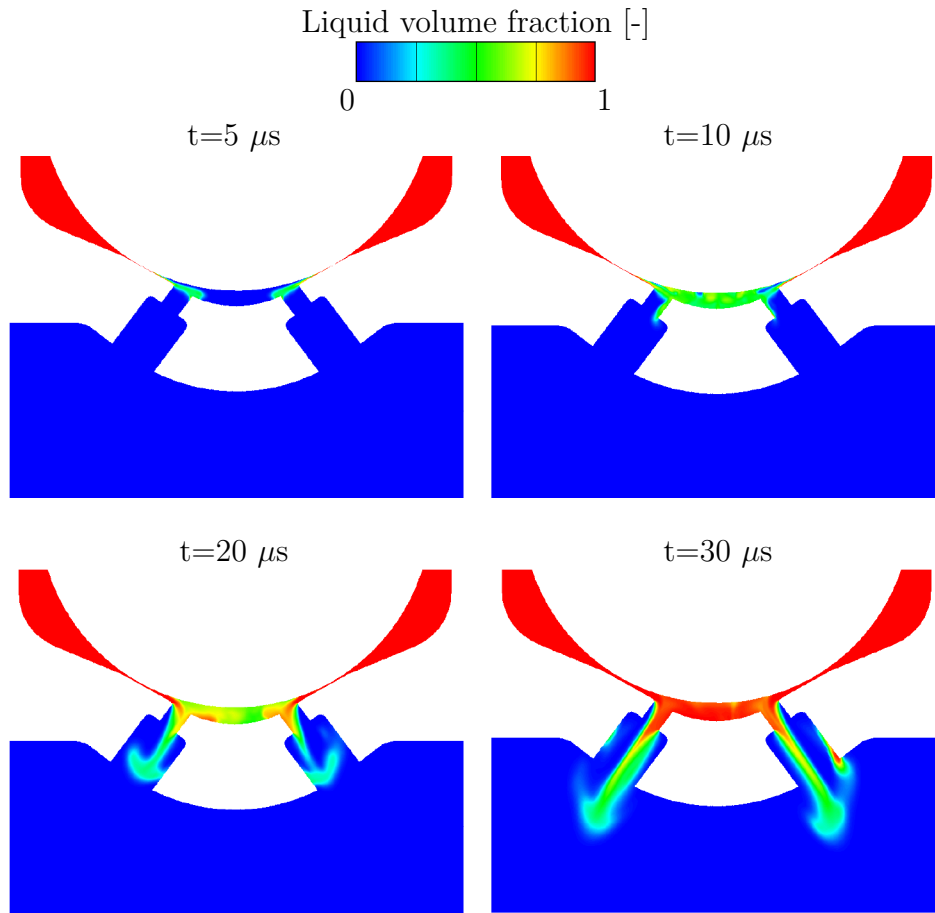


Figure 4.6: Standard Spray G liquid phase volume fraction at the early stage of injection

When the injection process enters the stabilization phase, the volume fraction field settles and fluctuations vanish. On the other hand, the variations in flow between individual nozzles have been captured. The result of nozzle holes imperfections has been given in Figure 4.8. Figure 4.9 shows the fuel vapour volume fraction at the early stage of injection. In the standard Spray G simulations, the vapour phase is present in traces along the injector wall. As it can be observed, after a short period, the presence of vapour fades. Compared to the liquid fuel, its volume fraction and especially the mass are negligible.

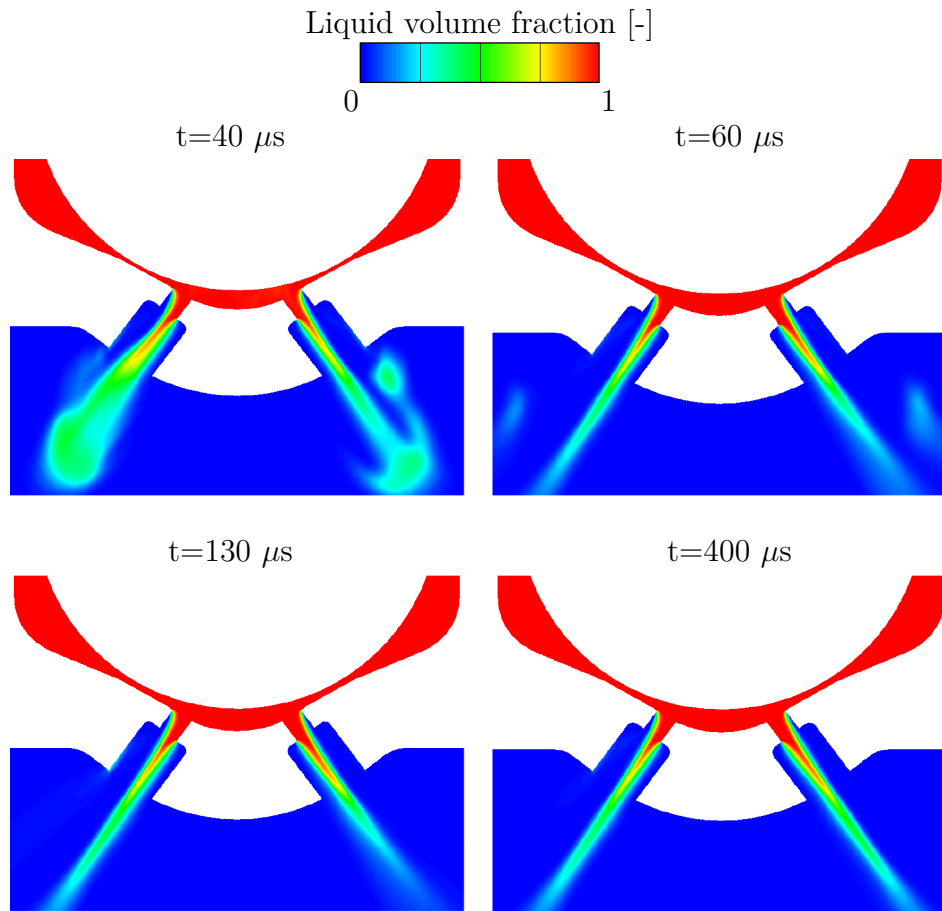


Figure 4.7: Spray G liquid phase penetration

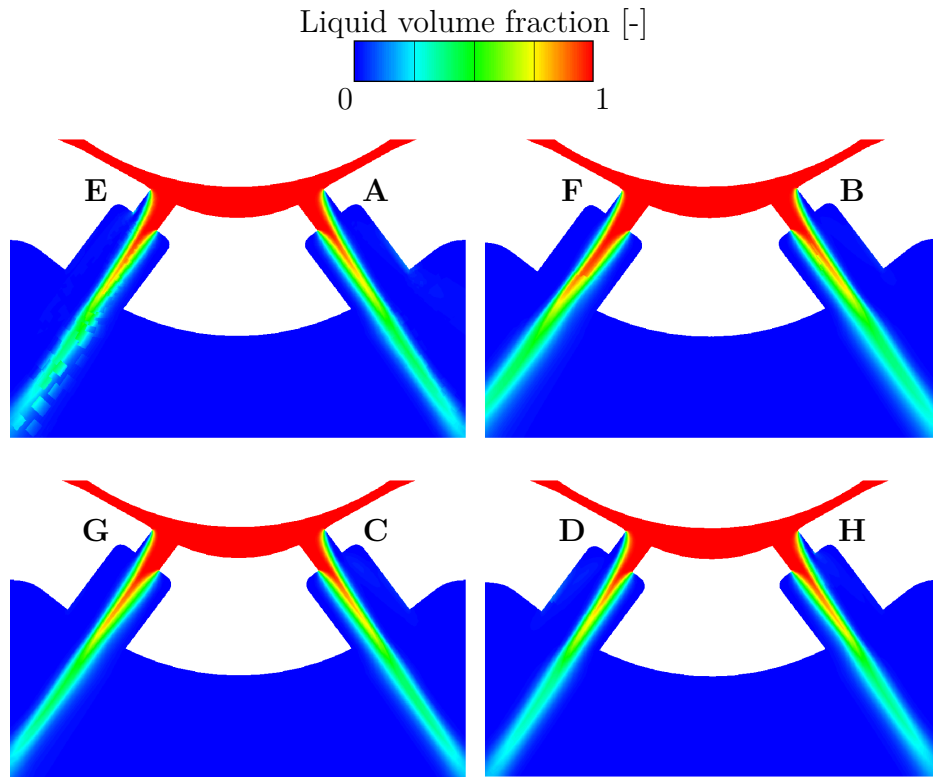


Figure 4.8: Standard Spray G operating condition: hole-to-hole variation taken for the liquid phase at 400  $\mu\text{s}$  after the start of the injection

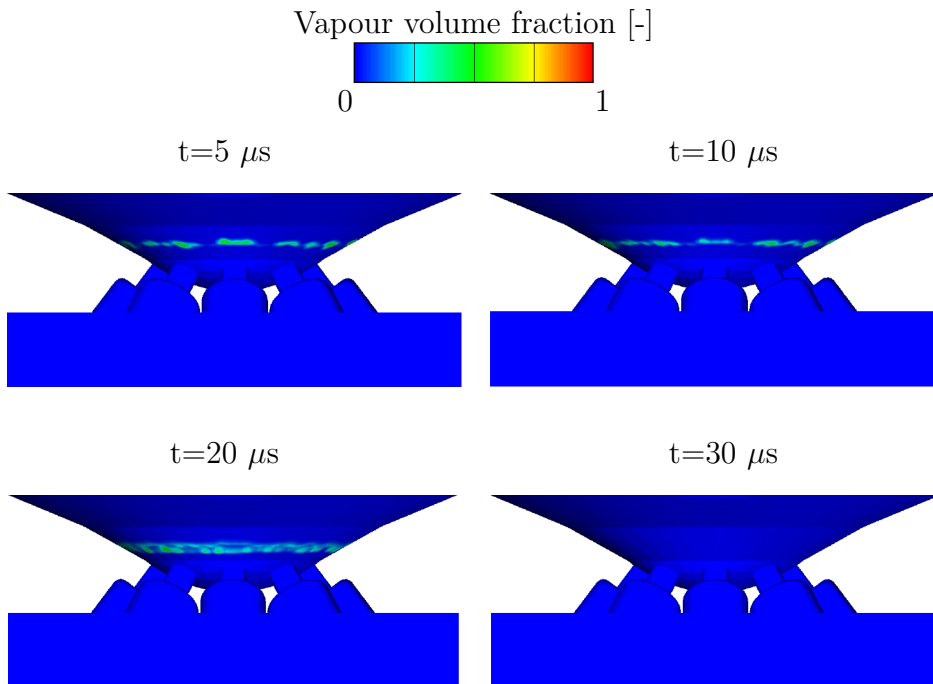


Figure 4.9: Standard Spray G vapour volume fraction at the early stage of injection

In addition, development of the liquid phase velocity field is given in Figure 4.10. Development of the velocity field progresses similar to the evolution of the liquid fuel volume fraction. Instant velocity increase is seen from the moment needle starts to lift. As flow develops, the maximum velocity value stabilizes around the nozzle hole axis, thus helping the fast fuel penetration through the discharge volume. In the late stage of the injection process, the velocity field stabilizes and continues showing alike behaviour with slight fluctuations.

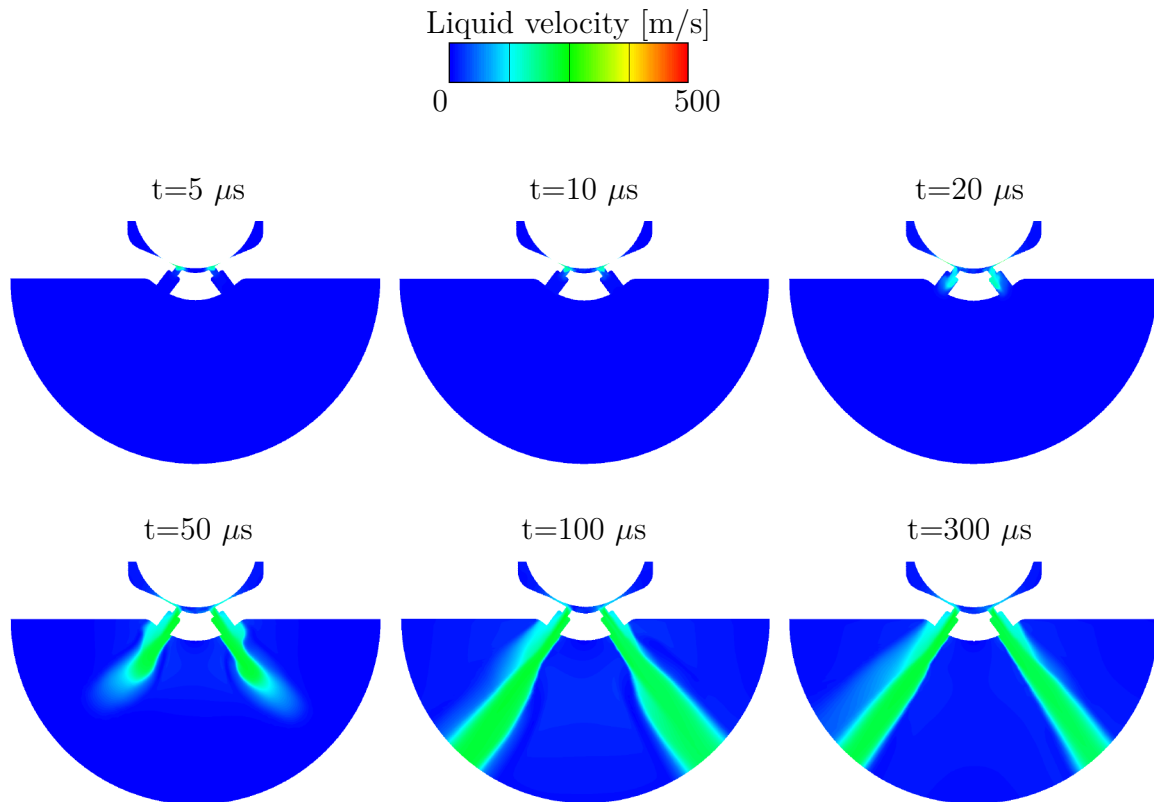


Figure 4.10: Spray G liquid phase velocity field

Finally, results conducted from Spray G2 simulations are presented. Figure 4.11 shows a development of a liquid phase volume fraction at the early stage of injection process under the flash boiling operating conditions. Before the liquid enters the nozzles, recirculation of the flow is evident. Afterwards, similar to the Spray G case, a large turning angle at the nozzle entrance leads to flow separation within the nozzle hole, hence decreasing the effective nozzle hole cross-section. Once the flow field adopts its developed state, it can be noticed that the liquid fuel axis has a tendency to shift towards the injector body axis.

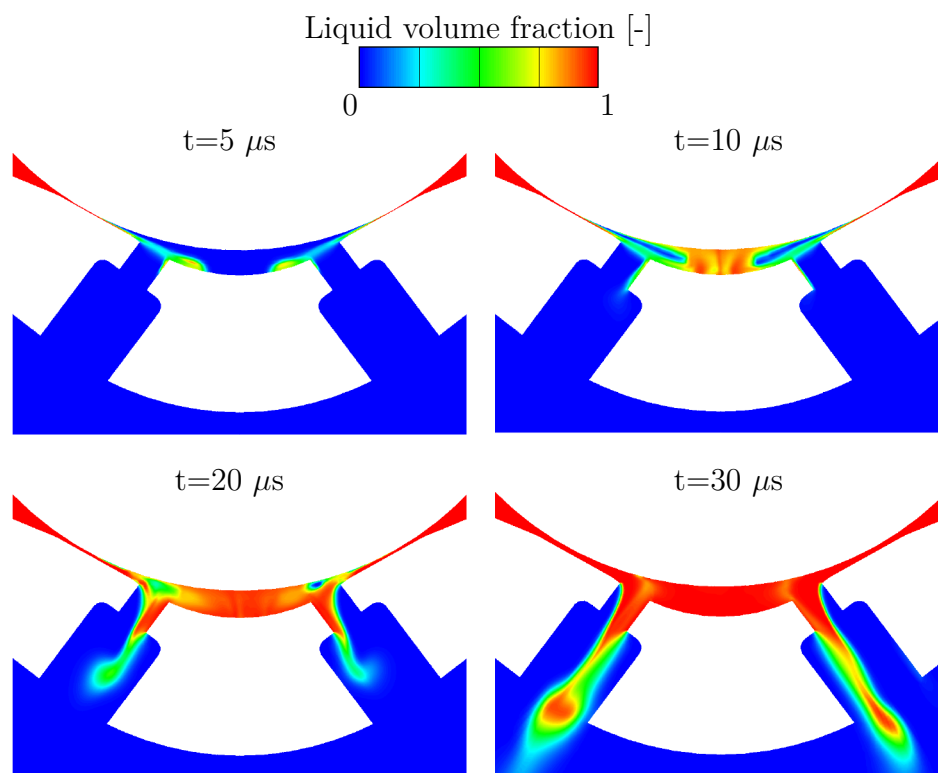


Figure 4.11: Spray G2 liquid phase volume fraction at early stage of injection

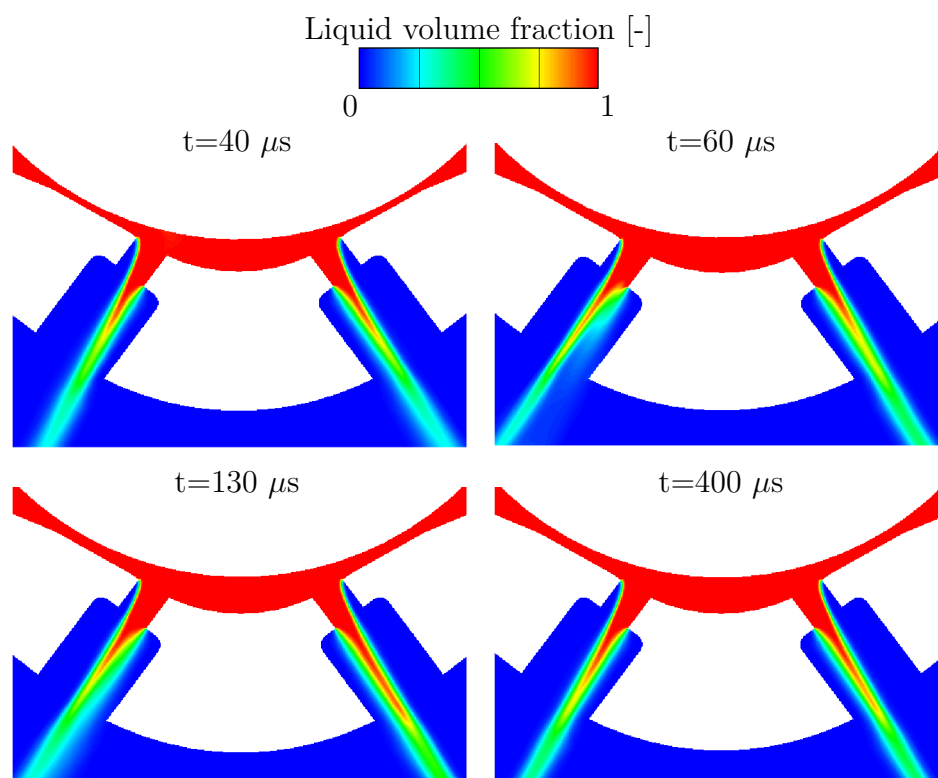


Figure 4.12: Spray G2 liquid phase development

Compared to the standard Spray G case, the plume deflection angle is greater in the flash boiling simulation. Moreover, the flow field settles in its developed state with minor fluctuations. When observing the development of the velocity field through the injection process, shown in Figure 4.13, it is clear that fuel quickly reaches velocity values greater than the maximum velocity value in the standard Spray G case. Reason for that is ten times lower pressure initialized within the sac, nozzles and discharge volume. High-velocity area, that can be seen in the capture taken at  $50 \mu\text{s}$  after the start of injection, is also a low-pressure area where the liquid fuel vaporizes. Despite the liquid volume fraction displayed in Figure 4.11, where the liquid phase takes only one part of total counterbore value, the liquid fuel is present in the complete counterbore, although in very small volume fraction.

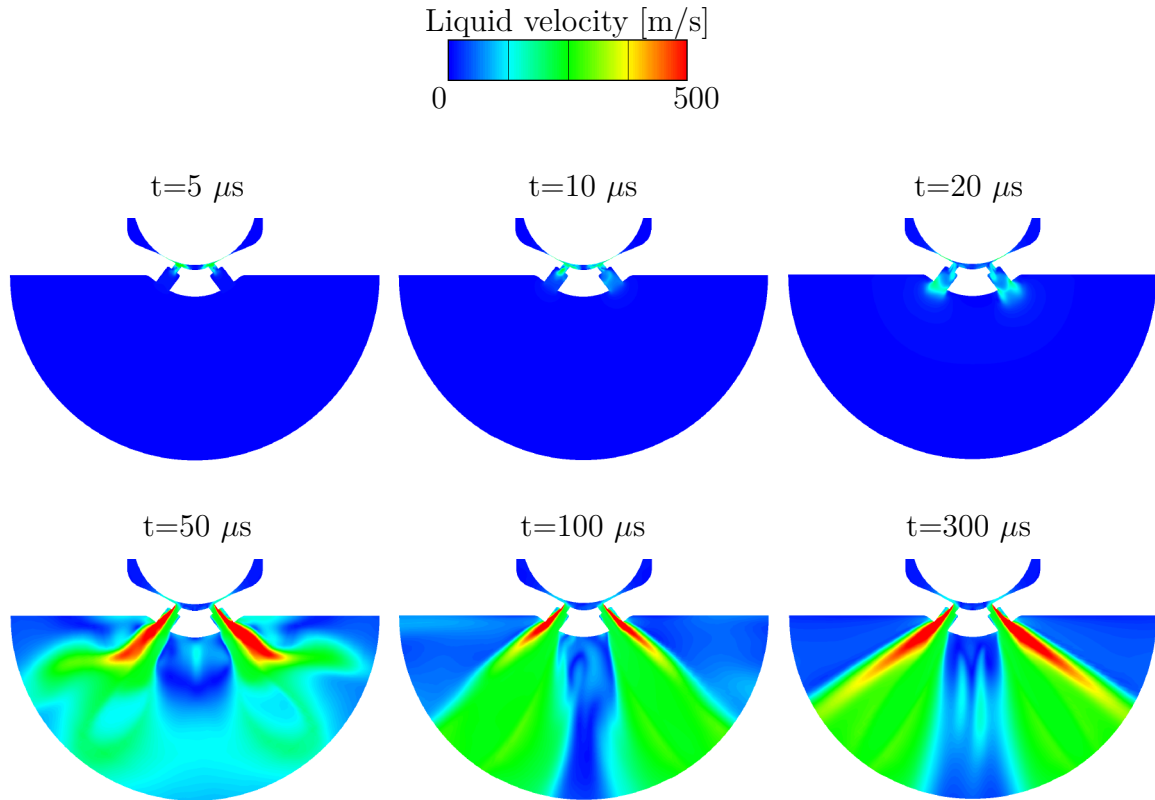


Figure 4.13: Spray G2 liquid phase velocity field

In the flash boiling simulation, a special attention has been dedicated to the investigation of the vapour phase. As explained in the introduction, the main effect of the flash boiling condition is the generation of large amount of fuel vapour. Therefore, the development of the fuel vapour volume fraction is shown in Figure 4.14.

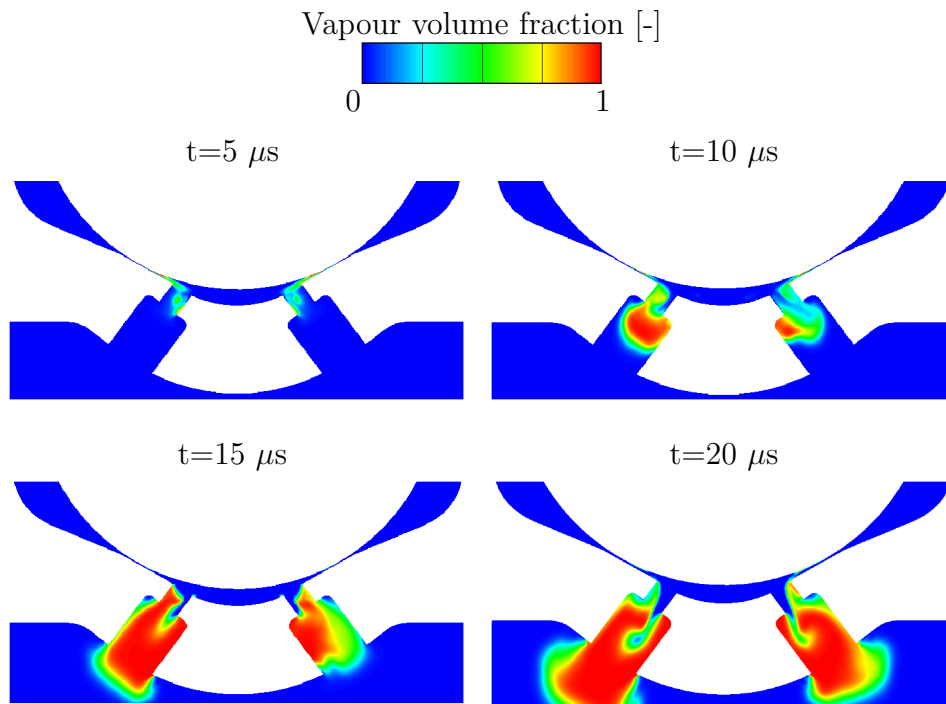


Figure 4.14: Spray G2 vapour volume fraction at the early stage of injection

Presence of the vapour phase is evident shortly after the needle starts to lift ( $5 \mu s$ ), as shown in Figure 4.14, which leads to the conclusion that fuel vaporization under the flash boiling operating mode happens almost immediately. Hence, the vaporized fuel propagates faster than the phase 1, i.e. liquid fuel, which is obvious if comparing figures 4.11 and 4.14. As it vaporizes, the fuel vapour occupies the complete counterbore volume. The vapour spreading is limited by the nozzle geometry, and when it reaches the combustion chamber, a rapid expansion of vapour occurs. Further development of the vaporized fuel is represented in Figure 4.15, where the vapour volume fraction for the complete computational domain can be seen. Fast spreading of the vapour cloud inside the discharge volume indicates flow recirculation as it hits the domain boundaries. The composition of the plumes consists of a liquid fuel core, which occupies most of the nozzle holes and is getting more diluted as it penetrates further in the counterbores, where the vaporization process acts. In continuation, the developed state of vapour volume fraction field is displayed. Figure 4.15 hence shows the volume fraction of vaporized fuel at the maximum needle lift position. Since the plume angles are large and the distance between the neighbouring holes is small, it is expected that interaction between the neighbouring spray plumes appears. As it was previously discussed, plume-to-plume interaction plays



a significant role in the mass flow rate distribution.

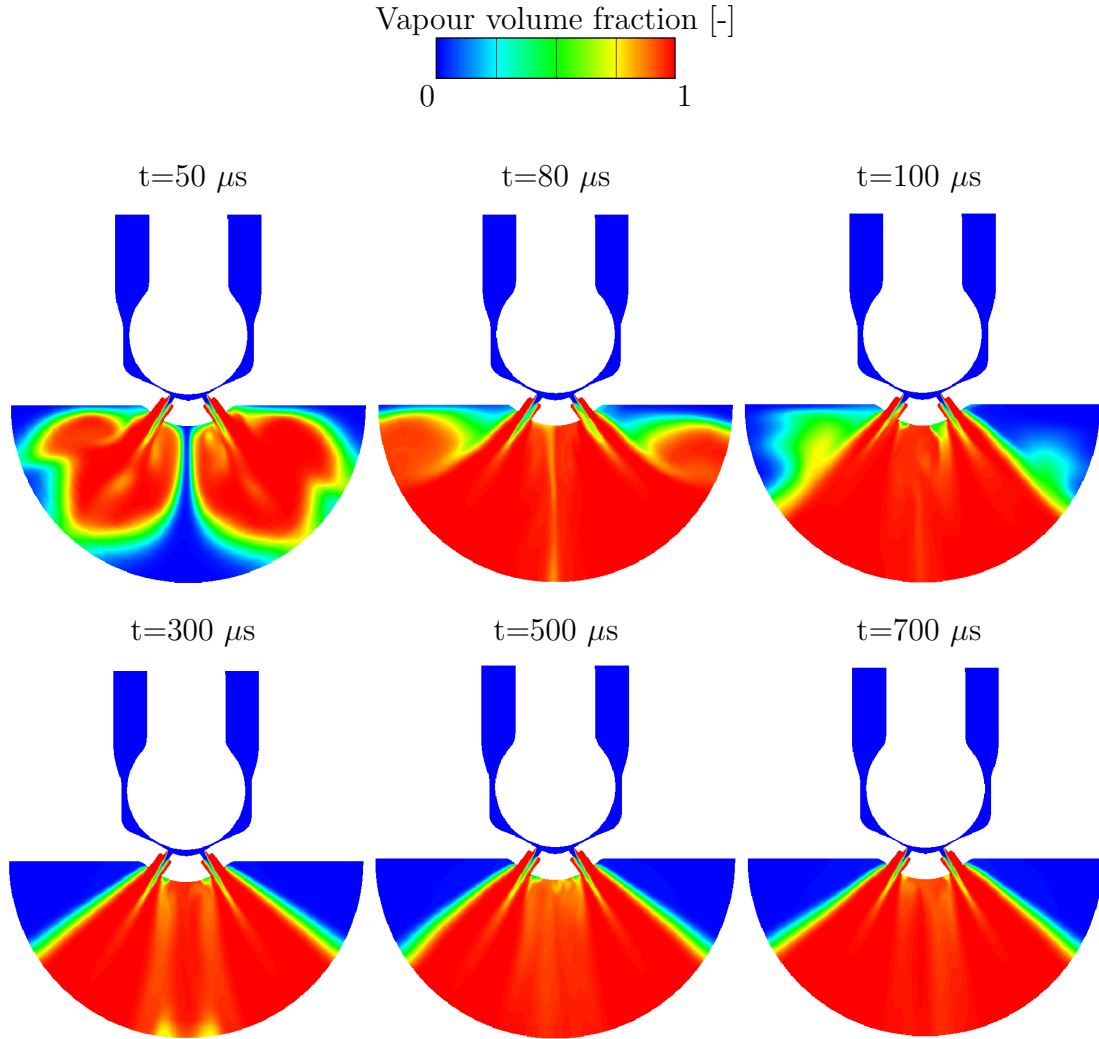


Figure 4.15: Development of a Spray G2 vapour phase volume fraction

Development of the vapour velocity of the performed flash-boiling simulation is shown in Figure 4.16. In this figure, three time steps of first half of the injection process are given. Again, gas is spreading with a high velocity that is the most pronounced on the outer side of the plumes and decreases towards the injector body axis. Thus, the value of the velocity at the inter-plume boundary is very low. Furthermore, in its stabilized phase, velocity distribution between the plumes follows a similar behaviour with minor fluctuations due to the nozzle interactions. Vapour velocity field, given in Figure 4.13, shows almost identical behaviour as the liquid phase velocity obtained from the flash boiling simulation.

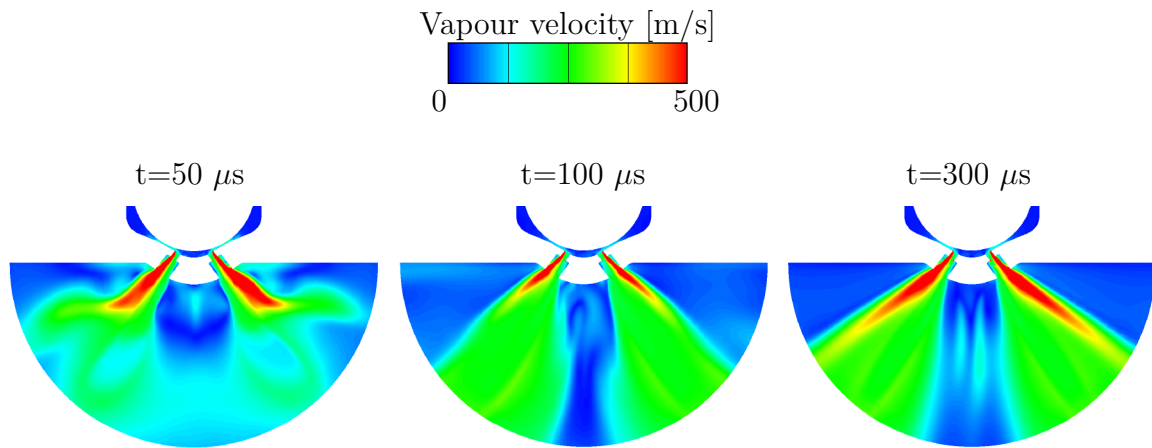


Figure 4.16: Spray G2 vapour phase velocity at the first half of injection process

Additionally, numerical results are compared with experimental imaging of ECN GDI spray penetration together with the numerical simulations carried out in [7] and [8]. Figure 4.17 shows a vapour phase obtained from the numerical simulation in comparison with the spray imaging given in [7]. Numerical results are in a good agreement with the experiment. Exiting plume angles are large in both cases and result in significant plume-to-plume interaction. Also, vapour uniformly contacts the outer edge of the counterbores and injector tip which is visible both in the simulation and experimental results. As a result, a thin liquid film forms on the outer side of injector tip after the injection process finishes.

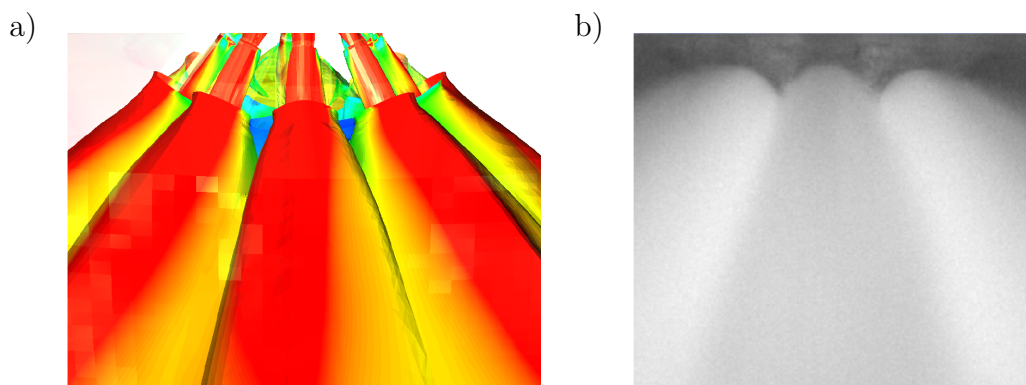


Figure 4.17: a) Iso-surface of vapour volume fraction taken in the middle of simulation ( $t=400 \mu s$ ), b) experimental imaging [7]

The comparison of the generated vapour is also made with the results of OpenFOAM simulation carried out by Baldwin [7]. Near the end of the simulation (at  $760 \mu s$  after the

start of the injection), a vertical plane surface cut is made in order to directly compare the two calculations, shown in Figure 4.18.

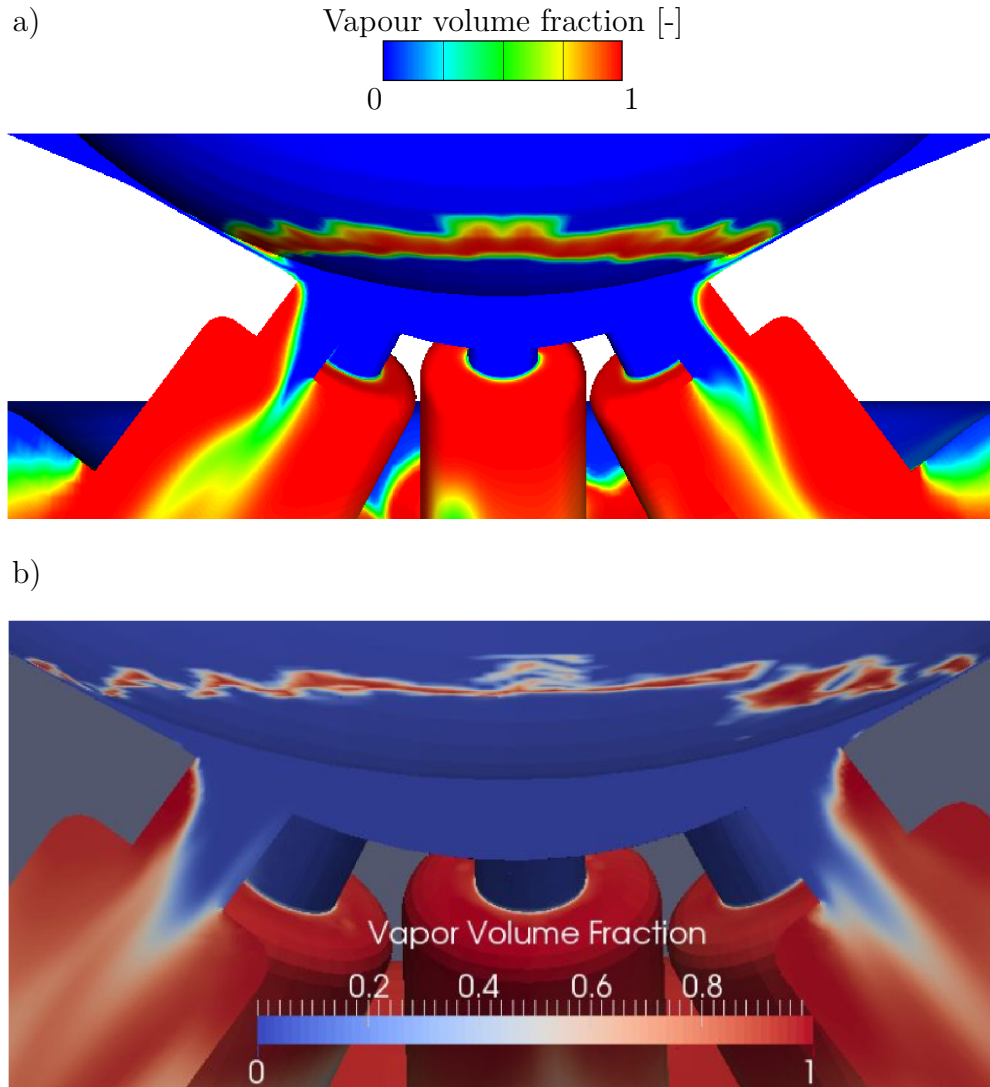


Figure 4.18: Vapour generated at low lift conditions near the end of injection at  $760 \mu\text{s}$  in Spray G2 simulation performed in: a) FIRE AVL<sup>TM</sup>, b) OpenFOAM [7]

The results are in a good agreement, showing alike vapour distribution within nozzles, as well as within the sac where the string-cavitation appearance can be seen, also shown in Figure 4.19. String-cavitation is a name for an unsteady vapour structure occurring upstream of the injection holes, inside the nozzle volume. According to [35], a string forming region is found to be at the core of recirculation zones. “Strings” ensue from the pre-existing cavitation forming at the sharp inlet nozzle corners. Researchers also established that the appearance of the cavitation strings is a function of several

parameters: needle lift, nozzle hole geometry, cavitation and Reynolds number. One of the main consequences of that kind of cavitation is increased vapour fraction inside the nozzle hole which reads as the reduction in the individual nozzle flow rate.

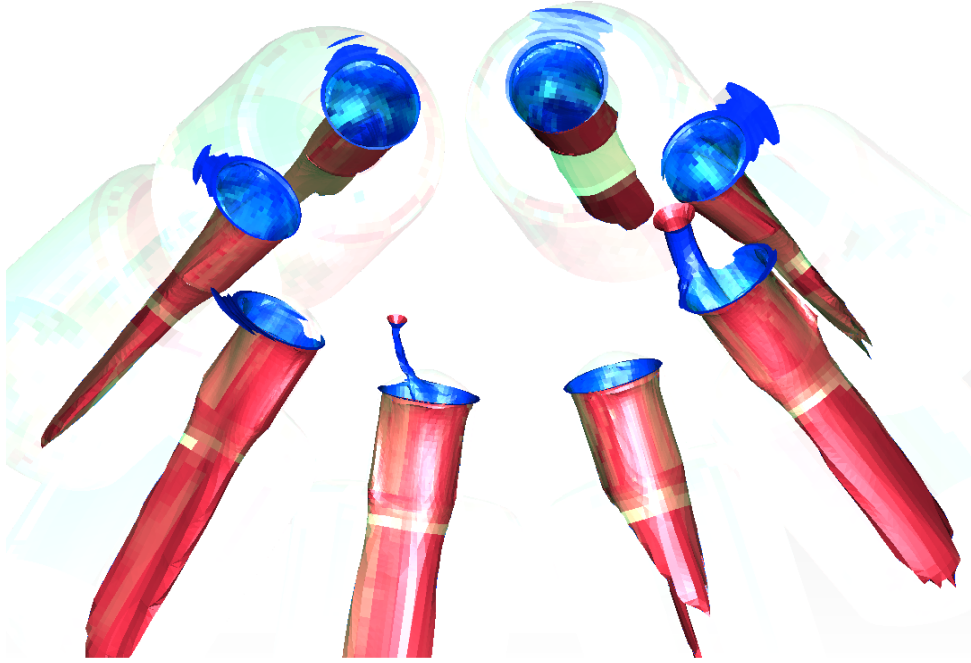


Figure 4.19: String-cavitation appearance in the upper nozzle region

In the end, the results of a flash boiling model are compared with the injection process under the standard operating mode.

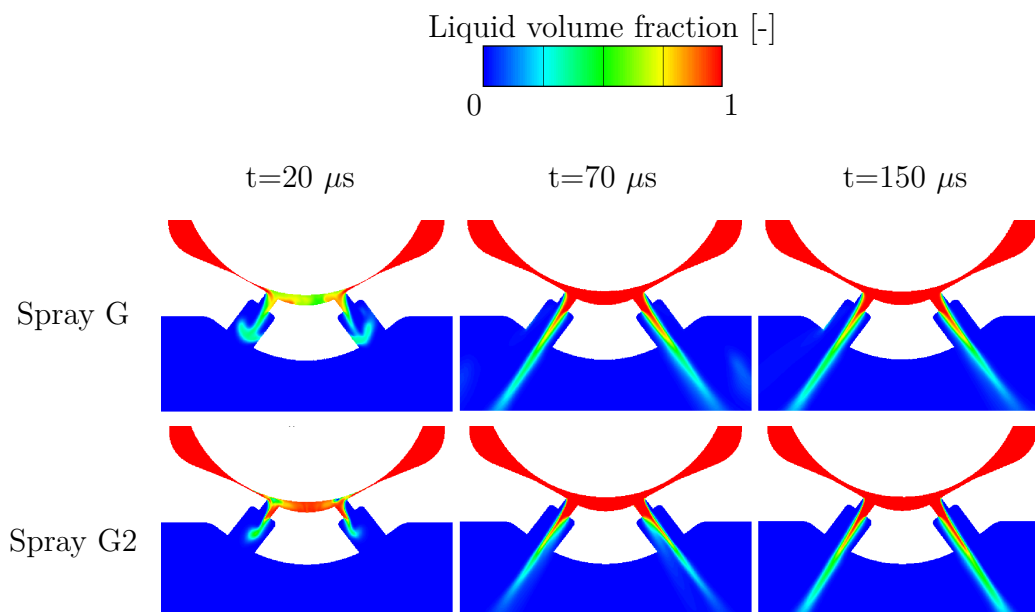


Figure 4.20: Liquid volume fraction comparison of Spray G and Spray G2 simulations

Figure 4.20 represents a liquid fuel volume fraction collected from both simulations, Spray G and Spray G2. It can be seen that in both cases, similar volume fraction distribution is kept. Before the flow develops, at the beginning of the injection process, fluctuations are visible.

A comparison of the vapour volume fraction is given in Figure 4.21. In the standard Spray G simulation, vapour can be noticed periodically with a small volume fraction value. Compared with the flash boiling case, the amount of vapour in the standard case is negligible. On the other hand, fuel vaporization in flash boiling condition happens immediately. As soon as vapour exits counterbores, rapid expansion occurs, and vapour is spreading through the entire domain.

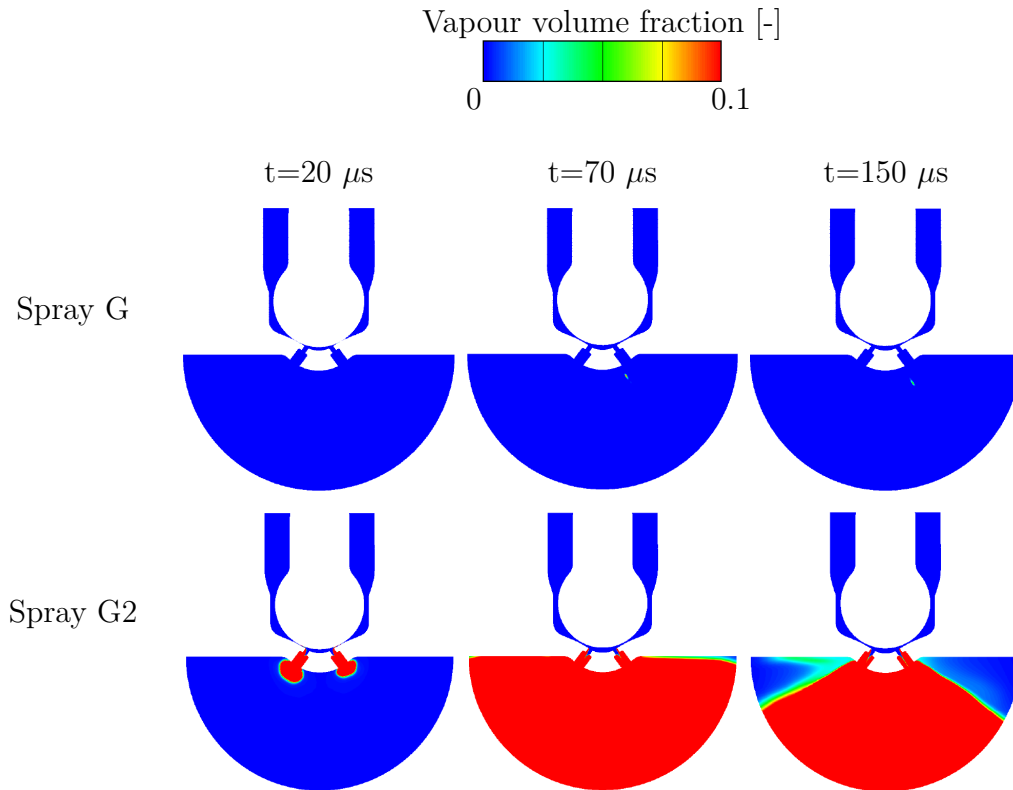


Figure 4.21: Vapour volume fraction comparison of Spray G and Spray G2 simulations

## 5 Conclusion

Deep understanding of all processes that are taking place within the internal combustion engines is necessary for the continuation of its improvement. One of such processes—the fuel injection—was thoroughly investigated in this thesis. With the usage of Computational Fluid Dynamics (CFD), a modern engineering tool that enables investigation of various engineering solutions in a short period of time, a direct fuel injection system under the flash boiling operating conditions was analysed. In order to recreate the actual movement of injector parts, a moving computational domain was generated according to experimentally obtained geometry of an ECN injector.

Calculations of the fuel injection process were performed in the commercial CFD software AVL FIRE<sup>TM</sup>, where two operating conditions were taken into consideration: standard and flash boiling. Comparison of the results in terms of mass flow rate, volume fraction and velocity was carried out. Numerical simulations mildly overestimated the values of injected fuel mass flow when compared to the experiment, which is attributed to neglecting the needle wobbling as well as geometry simplifications. Liquid phase in both cases showed similar behaviour in its volume fraction distribution, and in development of the velocity field. Vapour phase in the standard case appears periodically with its small volume fraction value, which is insignificant compared to the flash boiling simulation. A large amount of vapour is present under the flash boiling operating conditions. Rapid spreading of a spray cloud and the resulting interaction among the neighbouring plumes is also evident. Furthermore, flash boiling results were compared to an experiment and to a numerical simulation carried out in a different computational code. Good agreement was observed.

With the investigation of two operating modes of the direct injection system, many advantages of such processes were ascertained. It can be stated that the direct fuel

injection system offers satisfactory control over the ignition mixture, improving the combustion process, and consequently, the engine efficiency and performance. It is a technology that is experiencing a large-scale development since it showed to be the most promising solution for reducing emissions. Conclusively, it is safe to say that the direct fuel injection systems will find their way back to the general aviation someday.

# Bibliography

- [1] Sher, E., Bar-Kohany, T., Rashkovan, A.. Flash-boiling atomization. Progress in Energy and Combustion Science 2008;34(4):417–439. doi:10.1016/j.pecs.2007.05.001.
- [2] Kawano, D., Ishii, H., Suzuki, H., Goto, Y., Odaka, M., Senda, J.. Numerical study on flash-boiling spray of multicomponent fuel. Heat Transfer - Asian Research 2006;35(5):369–385. doi:10.1002/htj.20117.
- [3] Plesset, M.S., Prosperetti, A.. Bubbe Dynamics and Cavitation. Annual Reviews of Fluid Mechanics 1977;9:145–185. doi:10.1146/annurev.fl.09.010177.001045.
- [4] AVL Fire Documentation, v2017. 2017.
- [5] Engine Combustion Network, Spray G Geometry. URL: <https://ecn.sandia.gov/gasoline-spray-combustion/computational-method/mesh-and-geometry/>. Sep. 2018.
- [6] Engine Combustion Network, Spray G Operating Conditions. URL: <https://ecn.sandia.gov/gasoline-spray-combustion/target-condition/spray-g-operating-condition/>. Sep. 2018.
- [7] Baldwin, E.T., Grover, R.O., Parrish, S.E., Duke, D.J., Matusik, K.E., Powell, C.F., et al. String flash-boiling in gasoline direct injection simulations with transient needle motion. International Journal of Multiphase Flow 2016;87:90–101. doi:10.1016/j.ijmultiphaseflow.2016.09.004.
- [8] Moulai, M., Grover, R., Parrish, S., Schmidt, D.. Internal and Near-Nozzle Flow in a Multi-Hole Gasoline Injector Under Flashing and Non-Flashing Conditions. SAE Technical Paper 2015;01:0944. doi:10.4271/2015-01-0944.



- 
- [9] Lulić, Z., Mahalec, I., Kozarac, D.. Klipni motori I, Interna skripta. 2010.
- [10] Jurilj, I.. Avijacija i avion. Zagreb: Despot infinitus; 2014.
- [11] Fuel Injection Systems. URL: <http://okigihan.blogspot.com/p/float-type-carburetors-float-type.html>. Oct. 2018.
- [12] Carburettor working principle. URL: <https://www.experimentalaircraft.info/articles/aircraft-engine-carburetor.php>. Oct. 2018.
- [13] Lulić, Z., Mahalec, I., Kozarac, D.. Klipni motori II, Interna skripta. 2008.
- [14] Suma, S., Koizumi, M.. Internal Boiling atomization by Rapid Pressure Reduction of Liquids. Trans J-STAGE 1977;43:608–4621. doi:10.1299/kikai1938.43.4608.
- [15] Stansfield, P., Mojtabi, M., Wigley, G., Pitcher, G.. GDI Spray Propagation under a variety of Ambient and Engine Conditions. Engine Combustion Processes Conference 2007;.
- [16] Vanderwege, B.A., Hochgreb, S.. The effect of fuel volatility on sprays from high-pressure swirl injectors. Symposium (International) on Combustion 1998;27(2):1865–1871. doi:10.1016/S0082-0784(98)80029-5.
- [17] Mojtabi, M., Chadwick, N., Wigley, G., Helie, J.. The effect of flash boiling on break up and atomization in GDI sprays. ILASS 2008;:8–10.
- [18] Gebhard, P.. Zerfall und Verdampfung von Einspritzstrahlen aus lamellenbildenden Düsen 1966;:23–25.
- [19] Sato, K., Lee, C., Nagai, N.. A study on atomization process of superheated liquid. Trans JSME (B) 1984;:1743–1752.
- [20] Senda, J., Wada, Y., Kawano, D., Fujimoto, H.. Improvement of combustion and emissions in diesel engines by means of enhanced mixture formation based on flash boiling of mixed fuel. International Journal of Engine Research 2008;9(1):15–27. doi:10.1243/14680874JER02007.

- 
- [21] Mohan, B., Jaasim, M., Perez, F.H., Sim, J., Roberts, W., Im, H.. Internal and near nozzle flow simulations of gasoline multi-hole injector ( ECN Spray G ) with transient needle motion 2018;;7–12.
- [22] Saha, K., Som, S., Battistoni, M., Li, Y., Pomraning, E., Senecal, P.K.. Numerical Investigation of Two-Phase Flow Evolution of In- and Near-Nozzle Regions of a Gasoline Direct Injection Engine During Needle Transients. SAE International Journal of Engines 2016;9(2):2016–01–0870. doi:10.4271/2016-01-0870.
- [23] Saha, K., Som, S., Battistoni, M., Li, Y., Quan, S., Senecal, P.K.. Numerical simulation of internal and near-nozzle flow of a gasoline direct injection fuel injector. Journal of Physics: Conference Series 2015;656(1):7–11. doi:10.1088/1742-6596/656/1/012100.
- [24] Strek, P., Duke, D., Swantek, A., Kastengren, A., Powell, C.F., Schmidt, D.P.. X-Ray Radiography and CFD Studies of the Spray G Injector 2016;doi:10.4271/2016-01-0858.
- [25] Guo, H., Ding, H., Li, Y., Ma, X., Wang, Z., Xu, H., et al. Comparison of spray collapses at elevated ambient pressure and flash boiling conditions using multi-hole gasoline direct injector. Fuel 2017;199:125–134. doi:10.1016/j.fuel.2017.02.071.
- [26] Lacey, J., Poursadegh, F., Brear, M.J., Gordon, R., Petersen, P., Lakey, C., et al. Generalizing the behavior of flash-boiling, plume interaction and spray collapse for multi-hole, direct injection. Fuel 2017;200:345–356. doi:10.1016/j.fuel.2017.03.057.
- [27] Serras-Pereira, J., Van Romunde, Z., Aleiferis, P.G., Richardson, D., Wallace, S., Cracknell, R.F.. Cavitation, primary break-up and flash boiling of gasoline, iso-octane and n-pentane with a real-size optical direct-injection nozzle. Fuel 2010;89(9):2592–2607. doi:10.1016/j.fuel.2010.03.030.
- [28] Price, C., Hamzehloo, A., Aleiferis, P., Richardson, D.. Aspects of Numerical Modelling of Flash-Boiling Fuel Sprays 2015;doi:10.4271/2015-24-2463.
- [29] Hanjalić, K., Popovac, M., Hadžiabdić, M.. A robust near-wall elliptic-relaxation

- eddy-viscosity turbulence model for CFD. *International Journal of Heat and Fluid Flow* 2004;25(6):1047–1051. doi:10.1016/j.ijheatfluidflow.2004.07.005.
- [30] Karathanassis, I.K., Koukouvini, P., Gavaises, M.. Comparative evaluation of phase-change mechanisms for the prediction of flashing flows. *International Journal of Multiphase Flow* 2017;95:257–270. doi:10.1016/j.ijmultiphaseflow.2017.06.006.
- [31] Senda, J., Hojyo, Y., Fujimoto, H.. Modeling of atomization and vaporization process in flash boiling spray 1994;15:291–296. doi:10.4271/941925.
- [32] Mimouni, S., Denéfle, R., Fleau, S., Vincent, S.. Multifield Approach and Interface Locating Method for Two-Phase Flows in Nuclear Power Plant. *SimHydro* 2014;doi:10.1007/978-981-287-615-7\_33.
- [33] CFL Number. URL: <https://www.simscale.com/blog/2017/08/cfl-condition/>. Nov. 2018.
- [34] Payri, R., García, J.M., Salvador, F.J., Gimeno, J.. Using spray momentum flux measurements to understand the influence of diesel nozzle geometry on spray characteristics. *Fuel* 2005;84(5):551–561. doi:10.1016/j.fuel.2004.10.009.
- [35] Giannadakis, E., Gavaises, M., Arcoumanis, C.. Modelling of cavitation in diesel injector nozzles. *Journal of Fluid Mechanics* 2008;616:153–193. doi:10.1017/S0022112008003777.

# A | Appendix

## Matlab Code

```
1 %% Nozle file %%
2
3 format short e
4
5 fid_1=fopen('Nozzle_hole_1.nzf'); % upisati ime *.nzf
    dokumenta
6     % fileID
7     % varijabla pomocu koje funkcija textscan prolazi kroz
    dokument
8     % fid=fopen('naziv .nzf dokumenta')
9
10 calc_01=textscan(fid_1,'%f', 1, 'HeaderLines', 12, '
    CollectOutput', true, 'Delimiter', '', 'EmptyValue', 0);
11 x_01=cell2mat(calc_01);
12 phase_num=x_01; % broj faza
13
14 calc_02=textscan(fid_1,'%f', 1, 'HeaderLines', 38, '
    CollectOutput', true, 'Delimiter', '', 'EmptyValue', 0);
15 x_02=cell2mat(calc_02);
16 numOfTsteps=x_02; % broj vremenskih koraka
17
18 calc_03=textscan(fid_1,'%f', 1, 'HeaderLines', numOfTsteps+2, '
    CollectOutput', true, 'Delimiter', '', 'EmptyValue', 0);
```

```

        'CollectOutput', true, 'Delimiter', '', 'EmptyValue', 0);
19
20 Block=1;
21 while ~feof(fid_1)
22
23     % 'textscan' prolazi kroz dokument identificiran 'fid'
        varijablom.
24     % textscan(fid, 'tip podataka (floating number)', '
        naslovna linija',
25     % broj naslovnih linija koje zelimo preskociti,
26     % 'spremanje skeniranih podataka', 'razdjelnik podataka',
        '',
27     % 'prazne vrijednosti upisuje kao 0')
28
29 Alarge_calc_1(Block)=textscan(fid_1, '%f%f', 1, 'HeaderLines',
        1, 'CollectOutput', true, 'Delimiter', '', 'EmptyValue', 0);
30 Alarge_x1=Alarge_calc_1(cellfun(@isempty, Alarge_calc_1)==0);
        % Pronalazenje i eliminiranje
31                                     % praznih cell-ova
32 Alarge_x11=cell2mat(Alarge_x1(:, :)'); % Pretvaranje podataka
        iz array u matrice
33 t=Alarge_x11(:, 1); % Vremenski koraci zapisivanje podataka
34 numElements=Alarge_x11(1, 2); % Broj face-ova promatrane
        geometrije
35
36 Alarge_calc_2(Block)=textscan(fid_1, '%f%f%f', 1, '
        'CollectOutput', true, 'Delimiter', '', 'EmptyValue', 0);
37 Alarge_x2=Alarge_calc_2(cellfun(@isempty, Alarge_calc_2)==0);
38 Alarge_x22=cell2mat(Alarge_x2(:, :)');
39 m1_Alarge_mov=Alarge_x22(:, 1); % Maseni protok faze 1 [kg/s]
40 m2_Alarge_mov=Alarge_x22(:, 2); % Maseni protok faze 2
41 m3_Alarge_mov=Alarge_x22(:, 3); % Maseni protok faze 3

```

```

42
43 A_large_calc_3(Block)=textscan(fid_1, '%f%f%f%f%f%f%f',
    numElements, 'CollectOutput', true, 'Delimiter', ',', '
    EmptyValue', 0);
44 A_large_x3=A_large_calc_3(cellfun(@isempty, A_large_calc_3)==0);
45 A_large_x33=cell2mat(A_large_x3(:,:)');
46 x_cen_A_large=A_large_x33(:,1); % x koordinata sredista elementa
47 y_cen_A_large=A_large_x33(:,2); % y koordinata sredista elementa
48 z_cen_A_large=A_large_x33(:,3); % z koordinata sredista elementa
49 f_A_large=A_large_x33(1:numElements,4); % povrsina elementa
50 x_nor_A_large=A_large_x33(:,5); % x koordinata vektora normale
51 y_nor_A_large=A_large_x33(:,6); % y koordinata vektora normale
52 z_nor_A_large=A_large_x33(:,7); % z koordinata vektora normale
53
54 A_large_calc_4(Block)=textscan(fid_1, '%f%f%f%f%f%f%f',
    phase_num*numElements, 'CollectOutput', true, 'Delimiter',
    ',', 'EmptyValue', 0);
55 A_large_x4=A_large_calc_4(cellfun(@isempty, A_large_calc_4)==0);
56 A_large_x44=cell2mat(A_large_x4(:,:)');
57
58 A_large_calc_5(Block)=textscan(fid_1, '%f%f%*f%*f%*f%*f%*f',
    numElements, 'CollectOutput', true, 'Delimiter', ',', '
    EmptyValue', 0);
59 A_large_x5=A_large_calc_5(cellfun(@isempty, A_large_calc_5)==0);
60 A_large_x55=cell2mat(A_large_x5(:,:)');
61 S1_A_large=A_large_x55(:,1); S2_A_large=A_large_x55(:,2); % '
    attribute data'
62
63 Block=Block+1;
64 end
65
66 [~,~]=fclose(fid_1);

```

```

67
68 numberOfTimesteps=numOfTsteps; % Broj vremenskih koraka
69 numberOfPhases=phase_num;
70 numberOfFaces=numOfElements;
71 % u v w k epsilon ro alfa T
72
73 % Koristenje: red cell arraya oznacava timestep, stupac fazu; u
    {2,3} – faza
74 % 3 timestepa 2 varijable u
75
76 for timestep=1:numberOfTimesteps % loop po timestepu
77     for phase=1:numberOfPhases % loop po fazi
78         index=(numberOfPhases*numberOfFaces)*(timestep-1)+
            numberOfFaces*(phase-1)+1; % Prvi clan niza od N
            faceova
79         u_Alarge{timestep, phase}=A_large_x44(index:index+
            numberOfFaces-1,1);
80         v_Alarge{timestep, phase}=A_large_x44(index:index+
            numberOfFaces-1,2);
81         w_Alarge{timestep, phase}=A_large_x44(index:index+
            numberOfFaces-1,3);
82         k_Alarge{timestep, phase}=A_large_x44(index:index+
            numberOfFaces-1,4);
83         epsilon_Alarge{timestep, phase}=A_large_x44(index:index+
            numberOfFaces-1,5);
84         rho_Alarge{timestep, phase}=A_large_x44(index:index+
            numberOfFaces-1,6);
85         alpha_Alarge{timestep, phase}=A_large_x44(index:index+
            numberOfFaces-1,7);
86         T_Alarge{timestep, phase}=A_large_x44(index:index+
            numberOfFaces-1,8);
87     end

```

```

88 end
89
90 u_ph1_Alarge=[u_Alarge{:},1]; u_ph2_Alarge=[u_Alarge{:},2];
    u_ph3_Alarge=[u_Alarge{:},3]; % u komponenta brzine
    pojedine faze za sve timestep-ove (stupce)
91 v_ph1_Alarge=[v_Alarge{:},1]; v_ph2_Alarge=[v_Alarge{:},2];
    v_ph3_Alarge=[v_Alarge{:},3]; % v komponenta brzine %
    pojedine faze za sve timestep-ove (stupce)
92 w_ph1_Alarge=[w_Alarge{:},1]; w_ph2_Alarge=[w_Alarge{:},2];
    w_ph3_Alarge=[w_Alarge{:},3]; % w komponenta brzine %
    pojedine faze za sve timestep-ove (stupce)
93 k_ph1_Alarge=[k_Alarge{:},1]; k_ph2_Alarge=[k_Alarge{:},2];
    k_ph3_Alarge=[k_Alarge{:},3]; % 'turbulence kinetic energy'
    pojedine faze za sve timestep-ove (stupce)
94 epsilon_ph1_Alarge=[epsilon_Alarge{:},1]; epsilon_ph2_Alarge=[
    epsilon_Alarge{:},2]; epsilon_ph3_Alarge=[epsilon_Alarge
    {:},3]; % 'dissipation rate' pojedine faze za sve timestep-
    ove (stupce)
95 rho_ph1_Alarge=[rho_Alarge{:},1]; rho_ph2_Alarge=[rho_Alarge
    {:},2]; rho_ph3_Alarge=[rho_Alarge{:},3]; % gustoca
    pojedine faze za sve timestep-ove (stupce)
96 alpha_ph1_Alarge=[alpha_Alarge{:},1]; alpha_ph2_Alarge=[
    alpha_Alarge{:},2]; alpha_ph3_Alarge=[alpha_Alarge{:},3]; %
    volumni udio pojedine faze za sve timestep-ove (stupce)
97 T_ph1_Alarge=[T_Alarge{:},1]; T_ph2_Alarge=[T_Alarge{:},2];
    T_ph3_Alarge=[T_Alarge{:},3]; % temperatura pojedine faze
    za sve timestep-ove (stupce)

```